

The Sunyaev-Zeldovich Effect in CMB-calibrated theories applied to the Cosmic Background Imager anisotropy power at $\ell > 2000$

J. R. Bond,¹ C. R. Contaldi,¹ U.-L. Pen,¹ D. Pogosyan,² S. Prunet,³ M. I. Ruetalo,^{1,4} J. W. Wadsley,⁵ P. Zhang,^{1,4} B. S. Mason,^{6,7} S. T. Myers,⁸ T. J. Pearson,⁶ A. C. S. Readhead,⁶ J. L. Sievers,⁶ and P. S. Udomprasert⁶

ABSTRACT

We discuss the nature of the possible high- ℓ excess in the Cosmic Microwave Background (CMB) anisotropy power spectrum observed by the Cosmic Background Imager (CBI). We probe the angular structure of the excess in the CBI deep fields and investigate whether the origin of the excess could be due to the scattering of CMB photons by hot electrons within clusters, the Sunyaev-Zeldovich (SZ) effect. We estimate the density fluctuation parameters for amplitude, σ_8 , and shape, Γ , from CMB primary anisotropy data and other cosmological data. We use the results of two separate hydrodynamical codes for Λ CDM cosmologies, consistent with the allowed σ_8 and Γ values, to quantify the expected contribution from the SZ effect to the bandpowers of the CBI experiment and pass simulated SZ effect maps through our CBI analysis pipeline. The result is very sensitive to the value of σ_8 , and is roughly consistent with the observed power if $\sigma_8 \approx 1$. We conclude that the CBI anomaly could be a result of the SZ effect for the class of Λ CDM concordance models if σ_8 is in the upper range of values allowed by current CMB and Large Scale Structure (LSS) data.

Subject headings: cosmic microwave background — cosmology: observations

¹Canadian Institute for Theoretical Astrophysics, 60 St. George Street, Toronto Ontario M5S 3H8

²Physics Department, University of Alberta, Edmonton, Canada

³Institut d'Astrophysique de Paris, 98bis Boulevard Arago, F 75014 Paris, France

⁴Department of Astronomy and Astrophysics, University of Toronto, 60 St. George Street, Toronto Ontario M5S 3H8

⁵Department of Physics and Astronomy, McMaster University, Hamilton, ON L8S 4M1, Canada

⁶California Institute of Technology, 1200 East California Boulevard, Pasadena, CA 91125

⁷National Radio Astronomy Observatory, P.O. Box 2, Green Bank, WV 24944

⁸National Radio Astronomy Observatory, P.O. Box O, Socorro, NM 87801

1. Introduction

The Cosmic Background Imager (CBI) provides some of the highest resolution observations of the cosmic microwave background that have been made thus far. The observations cover the multipole range $400 < \ell < 4000$ which corresponds to collapsed masses ranging from a factor ten larger than the local group to the largest superclusters. These observations show, for the first time, the fluctuations on scales which gave rise to galaxy clusters and the damping of the power on small scales (Silk 1968; Peebles & Yu 1970; Bond & Efstathiou 1987). Together with the results of other recent, high precision, CMB experiments (Miller et al. 1999; Netterfield et al. 2002; Lee et al. 2001; Halverson et al. 2001) the observations appear to fit the scenario of adiabatic fluctuations generated by a period of inflationary expansion. The CBI observations also provide a unique insight into angular scales where secondary anisotropy effects are thought to become an important contribution to the power spectrum.

In a series of companion papers we have presented the results from the first year of CMB observations carried out by the CBI between April and December 2000. A preliminary analysis of the data was presented in Padin et al. (2001, hereafter Paper I). In Mason et al. (2002, hereafter Paper II) the observations of three differenced $45'$ (FWHM) deep fields were used to measure the power spectrum to multipoles $\ell \lesssim 3500$ in wide bands $\Delta\ell \sim 600$. Pearson et al. (2002, hereafter Paper III) discussed the analysis of three sets of differenced $145' \times 165'$ mosaiced fields. Mosaicing gives a telescope a larger effective primary beam than that defined by the dish radii. This increases the resolution in the uv -plane due to the smaller width of the convolving function. It also reduces the effect of cosmic variance on the errors by increasing the sampled area. The mosaic fields provide high signal-to-noise ratio measurements of the power spectrum up to multipoles $\ell \sim 1700$ with a resolution $\Delta\ell = 200$. Myers et al. (2002, hereafter Paper IV) give a detailed description of our correlation analysis and band power estimation methods. These have enabled us to analyze efficiently the large data sets involved in the CBI measurements. The implications of the results on cosmological parameters are described in Sievers et al. (2002, hereafter Paper V).

Results from the deep field observations show a fall in the power spectrum up to $\ell \sim 2000$ which is consistent with the damping tail due to the finite width of the last scattering surface. Beyond $\ell \sim 2000$ the power observed is higher than that expected from standard models of damped adiabatic perturbations which provide excellent fits to the data at larger scales. An extensive set of tests have been carried out to rule out possible systematic sources of the measured excess (Paper II). Paper III also reports results in this ℓ -range which are consistent with those of Paper II. Since the thermal noise levels in the CBI mosaic are substantially higher in this regime than in the deep field observations, the current discussion will focus on the deep field results.

Although the significance of the excess power is not conclusive it provides tantalizing evidence for the presence of secondary contributions to the microwave background anisotropies. One of the strongest expected secondary signals is the signature of the scattering of CMB photons by hot electrons in clusters known as the Sunyaev-Zeldovich (SZ) effect (Sunyaev & Zeldovich 1970).

The scattering leads to spectral distortions and anisotropies in the CMB. At the CBI observing frequencies the net effect is a decrement in the temperature along the line of site. The SZ effect is expected to dominate over the primary anisotropies at scales of a few arcminutes.

In this Paper we explore the possibility that the excess observed in the CBI deep fields may be a signature of the SZ effect. In § 2 we briefly review the CBI deep field result and present a Wiener filter as a method of component separation. In § 3 we describe the latest constraint on the normalization of the mass fluctuations σ_8 and shape parameter Γ from CMB experiments and a number of independent surveys. These parameters are critical in determining the amplitude of the SZ effect over the scales of interest to the CBI results. In § 4 we show the predicted power spectra for the SZ effect for various cosmological models. We use numerical methods to estimate the contribution from the SZ effect to the CMB power spectrum. In § 5 we use simulated CBI observations of SZ ‘contaminated’ CMB realizations to investigate the effect of a SZ foreground on our band power estimation methods. In § 6 we extend our image filtering to include specific templates for the SZ effect. Our results and conclusions are discussed in § 7.

2. The CBI Deep Field Power at $\ell > 2000$

In Paper II we report a measurement of Microwave Background anisotropies to $\ell = 3500$ derived from deep observations of three pairs of CBI pointings. These results show the power spectrum dropping to $\ell \sim 2000$, beyond which power levels are significantly higher than what is expected based on standard models for intrinsic CMB anisotropy. Assuming a single bin in flat bandpower above $\ell = 2010$ the observed signal is inconsistent with zero and best-fit models at the 3.5σ and 3.1σ levels respectively. The one and two sigma confidence intervals for this bandpower are $(359 \rightarrow 624) \mu\text{K}^2$ and $(199 \rightarrow 946) \mu\text{K}^2$, respectively, with a best-fit power level of $508 \mu\text{K}^2$. The confidence limits were obtained by explicitly calculating the asymmetric, non-Gaussian likelihood of the high- ℓ bandpower.

A key consideration in obtaining these results is the treatment of the discrete radio source foreground. Sources with positions known from low-frequency radio surveys were projected out of the data; the brightest sources were also measured at 31 GHz with the OVRO 40-m telescope and subtracted directly from the data. The OVRO data allowed a complementary treatment of this potentially limiting population, giving us great confidence in our bright source treatment. We estimated the power level due to sources too faint to appear in the low frequency radio source catalogs from 30 GHz number counts determined from CBI and OVRO data. The contribution of these residual sources is $114 \mu\text{K}^2$ —a factor of 4.5 below the observed excess—and we estimated an uncertainty of $\sim 57 \mu\text{K}^2$ in this contribution. The reader will find further discussion of both the CBI deep field spectrum and the treatment of the radio source foreground in Paper II.

The CBI does not have sufficient frequency coverage to strongly distinguish different signals by their frequency dependence (e.g., CMB, SZ, and Galactic foregrounds). Spectral separation of the

different components is therefore unfeasible. Although the sensitivity of the CBI results presented here is not sufficient to conclusively identify individual features in the maps, we present examples and simulations of a Wiener filtering technique described in Paper IV. We hope with future CBI observations and with the techniques demonstrated here to be able to identify conclusively the real features on the sky which are responsible for the excess.

The total mode to mode correlations in the data are separated into four components in a typical analysis of the deep field visibilities with the weight matrix \mathbf{W} as the sum

$$\mathbf{W} = (\mathbf{C}^N + \mathbf{C}^{CMB} + \mathbf{C}^{SRC} + \mathbf{C}^{res})^{-1}, \quad (1)$$

with noise (N), CMB, resolved sources (SRC) and residual source (res) components respectively. (In papers II and III, the resolved source contribution is split into two components, for sources with and without measured flux densities.)

In the limit where all the components can be considered Gaussian random fields we can define the probability of each signal given the data as the Gaussian (Bond & Crittenden 2002)

$$\ln P(\Delta^X | \bar{\Delta}) = -\frac{1}{2}(\Delta^X - \langle \Delta^X | \bar{\Delta} \rangle)^\dagger (\mathbf{C}^X)^{-1} (\Delta^X - \langle \Delta^X | \bar{\Delta} \rangle) - \frac{1}{2} \text{Tr} \ln \mathbf{C}^X - N \ln \sqrt{2\pi}, \quad (2)$$

where $\bar{\Delta}$ are the observations, Δ^X is the map vector of the component X, \mathbf{C}^X is the mode to mode correlation matrix for the component and N are the number of modes in the map. The mean $\langle \Delta^X | \bar{\Delta} \rangle$ defines the Wiener filtered map of the component given the observations

$$\Delta^X = \mathbf{C}^X \mathbf{W} \bar{\Delta}, \quad (3)$$

with variances

$$\langle \delta \Delta^X \delta \Delta^{X\dagger} | \bar{\Delta} \rangle = \mathbf{C}^X - \mathbf{C}^X \mathbf{W} \mathbf{C}^X. \quad (4)$$

In our case the maps Δ are column vectors containing the gridded visibility estimators (Paper IV) and sky plane maps can be obtained by Fast Fourier Transforming the estimators in the uv -plane. The correlation structure of the estimator grids are a necessary by-product of our gridding method and power spectrum estimation pipeline. The calculation of the correlations include all the relevant information on the sampling structure and convolution of the fine grained observation plane. Eq. 4 therefore includes all aspects of the uncertainties in the Wiener filtered map resulting from the observations.

We show an example of the use of such filters in Fig. 1. The sequence shows the result of applying different filters to the 08^h deep field observation. The original image (upper left) is first filtered to obtain a map of the total signal contributions which includes CMB and point sources (upper right). The CMB power spectrum obtained from the joint deep field analysis is then used as a template to obtain a map of the CMB contribution (lower left). The template includes the excess power above $\ell \sim 2000$. The post-subtraction residuals in the known point sources can also be separated into an image (lower right) which shows the total contribution of the modes which

are projected out when estimating the power spectrum. The mean Wiener filtered maps make no statement on the significance of any feature by themselves and considering only the mean can be misleading since there is no information on the allowed fluctuations around the mean in the map itself. This is particularly so in the case of interferometric observations where the nature of the noise and sampling uncertainties means that, although the power due to single features is conserved their structure in the sky plane is complicated by the extended nature of the correlations in the uncertainties. As shown above, however, in the Gaussian limit we can assign confidence limits on any features using Eq. 4.

A useful method of visualizing the significance of the features is by creating constrained realizations of the fluctuations and comparing these to the mean. For example we can obtain a random realization of the fluctuations by taking $\Delta_X^i = (\mathbf{C}^X - \mathbf{C}^X \mathbf{W} \mathbf{C}^X)^{1/2} \Delta^G$ where Δ^G are uniform, random Gaussian variates. Adding these maps to the mean we get an idea of the allowed fluctuations about the mean. Strongly constrained features will be relatively unaffected by the fluctuations and represent the high signal-to-noise ratio limit where $\mathbf{C}^X - \mathbf{C}^X \mathbf{W} \mathbf{C}^X \rightarrow 0$. Features measured at levels comparable to the “generalized” noise of the observations will be washed out by the fluctuation levels and represent the limit $\mathbf{C}^X - \mathbf{C}^X \mathbf{W} \mathbf{C}^X \rightarrow \mathbf{C}^X$. The full pixel-pixel covariance matrix of the component map can be calculated by direct FFT of the covariance matrix or by taking Monte Carlo ensemble averages of the fluctuation realizations.

The level of fluctuations allowed around the mean for the CMB component of Fig. 1 is shown in Fig. 2. The four panel figure shows the Wiener filter of the component and the same map with three random realizations of the fluctuations added to it. As expected the CMB component is well constrained on the scales shown in the image as the signal-to-noise ratio is high and the main features in the map are stable with respect to the fluctuations. The features are therefore expected to be closely related to “real” structures on the sky; but the nature of the observations means that the detailed structure of the features is not well constrained and most likely does not reflect the precise shape of the objects. The filtering of the large scale power by the interferometric observations also makes the correspondence with the large scale features on the sky not as intuitive as with sky plane based measurements. We will apply similar filters using specific models for the excess in § 5 and 6.

3. Amplitude and Shape Parameters for LSS from CMB Data

The SZ power spectrum has a strong dependence on the amplitude of the density fluctuations. The amplitude is usually parameterized by the rms of the (linear) mass fluctuations inside $8h^{-1}$ Mpc spheres, σ_8 . We now summarize the constraints we can obtain on the amplitude and shape of the matter power spectrum from CMB data and compare them to results from weak lensing surveys and cluster abundance data. Our parameter estimation pipeline also includes LSS priors which are designed to encompass the range in estimations from such experiments, as described below.

We use the parameter Γ to define the shape, following Bardeen, Bond, Kaiser, & Szalay (1986, hereafter BBKS) and Efstathiou et al. (1992, hereafter EBW). A byproduct of linear perturbation calculations used to compute \mathcal{C}_ℓ in our database are transfer functions for density fluctuations, which can be related to LSS observables. Various (comoving) wavenumber scales determined by the transport of the many species of particles present in the universe characterize these spectra. The most important scale for dark matter dominated universes is k_{Heq}^{-1} , that of the horizon at redshift Ω_m/Ω_{er} when the density in nonrelativistic matter, $\Omega_m \bar{a}^{-3}$, equals that in relativistic matter, $\Omega_{er} \bar{a}^{-4}$. This defines Γ_{eq} : $k_{\text{Heq}}^{-1} = 5 \Gamma_{eq}^{-1} h^{-1} \text{Mpc}$, where $\Gamma_{eq} = \Omega_m h [\Omega_{er}/(1.68\Omega_\gamma)]^{-1/2}$. For the cases we consider here, we simply have fixed the relativistic density to correspond to the photons and three species of very light neutrinos, so $\Gamma_{eq} = \Omega_m h$.

Certain functional forms for the transfer functions are popular: In EBW a form was adopted which fit a specific $\Omega_b = 0.03$ CDM model, but it is more general to adopt a fit to the $\Omega_b \rightarrow 0$ form given in BBKS appropriately corrected for the difference between the temperature of the CMB estimated then and known so well now (Bond 1996). Although the coefficients of fits to detailed models vary with ω_b, h, ω_m , which in particular result in oscillations in the transfer function for large ω_b/ω_m , it turns out that replacing Γ_{eq} by $\Gamma = \Gamma_{eq} \exp[-\Omega_b(1 + \Omega_m^{-1}(2h)^{1/2})]$ works reasonably well, to about 3% over the region most relevant to LSS (Sugiyama 1995; Bond 1996). Further, as shown in Bond (1994), replacing Γ by $\Gamma_{\text{eff}} = \Gamma + (n_s - 1)/2$ takes into account the main effect of spectral tilt over this LSS wavenumber band. It has also been shown that the Γ -models do fit the APM and 2dF data reasonably well at this stage. Particularly exciting is the prospect that the baryonic oscillations may be seen, but this is not required by the data yet. The approximate codification of a vast array of models in a single Γ_{eff} variable simplifies the treatment of LSS in the CMB data enormously.

The other variable we use to construct the LSS prior is the combination $\sigma_8 \Omega_m^{0.56}$. Although various fits to cluster abundances give slightly different exponents than the 0.56, the factor is consistent with a number of other measures and we adopt this form as a representative value. These invariably involve the biasing factor b_g for the galaxies involved. For example, relating the galaxy flow field to the galaxy density field inferred from redshift survey takes the form $[b_g \sigma_8] \beta_g$, where $\beta_g = \Omega_m^{0.56}/b_g$ is a numerical factor whose value depends upon data set and analysis procedure, that relates the biasing of the galaxies to σ_8 . A combination such as this also enters into redshift space distortions. A great advantage of the weak lensing and cluster abundance results shown in the figures is that they are independent of galaxy bias. However, for the cluster case, assumptions are needed which, as the spread in estimates indicates, lead to uncertainties.

In Figures 3, 4 and 5, we show the effect of the different priors on the distributions of σ_8 and $\sigma_8 \Omega_m^{0.56}$ respectively. We also compare these to weak lensing results of, from top to bottom, Hoekstra et al. (2002); van Waerbeke et al. (2002); Refregier et al. (2002); Bacon et al. (2002). The Hoekstra et al. (2002) and van Waerbeke et al. (2002) results correspond to a version of a weak prior: they marginalize over Γ_{eff} in the range 0.1 to 0.4, which is largely equivalent for this application to marginalization over ω_b , n_s and ω_m . They also marginalize over the uncertainty in the mean

redshift of the lensed galaxies z_s from 0.27 to 0.34 in the former case, and 0.78 to 1.08 in the latter case. On the other hand, the cosmology was kept fixed with $\Omega_m = 0.3$. Refregier et al. (2002) and Bacon et al. (2002) adopt a more restrictive parameter range. If the weak marginalization scheme of Hoekstra et al. (2002) and van Waerbeke et al. (2002) were used the error bars would increase.

The relation to cluster abundance estimates of σ_8 are discussed below. Figs. 3 and 4 show sample results of, from top to bottom, Eke et al. (1996); Carlberg et al. (1997); Fan & Bachall (1998); Pen (1998c); Pierpaoli, Scott & White (2001); Reiprich & Böhringer (2001); Seljak (2001); Viana, Nichol & Liddle (2001).

van Waerbeke et al. (2002) give a weak lensing result for $\Gamma_{\text{eff}} = 0.25 \pm 0.13$ with marginalization over Ω_m from 0.1 to 0.4 and over σ_8 . This is not explicitly plotted in Fig. 6 where we plot prior probabilities adopted for Γ_{eff} . The APM result is the long standing one used to construct the original prior, that Γ_{eff} in the 0.15 to 0.3 range provided a good fit to the data, e.g. EBW and Bond (1996). Recent 2dF (Peacock et al. 2001) and SDSS (Szalay et al. 2001) results shown give compatible results. Dodelson et al. (2001) estimate $0.14^{+0.11}_{-0.06}$, with errors at 95% confidence, for SDSS. Szalay et al. (2001) also give an estimate of σ_8 of 0.92 ± 0.06 , but the issue of galaxy biasing is folded into this determination. Although there are indications from the 2dF survey that biasing for the relevant galaxies is nearly unity from redshift-space distortions ($b = 1.04 \pm 0.11$, Verde et al. 2001), and the result is therefore compatible with the results shown, such results are not as directly applicable as those from cluster and lensing which directly relate to matter density power spectrum amplitudes.

The LSS prior used here and in Paper V involves a combination of constraints on the amplitude parameter $\sigma_8 \Omega_m^{0.56}$ and on the shape parameter Γ_{eff} . It differs slightly from that used in Lange et al. (2001), Jaffe et al. (2001) and Netterfield et al. (2002). We use $\sigma_8 \Omega_m^{0.56} = 0.47^{+0.02,+0.11}_{-0.02,-0.08}$, distributed as a Gaussian (first error) smeared by a uniform (tophat) distribution (second error). We constrain the shape of the power spectrum via $\Gamma_{\text{eff}} \equiv \Gamma + (n_s - 1)/2 = 0.21^{+0.03,+0.08}_{-0.03,-0.08}$, where $\Gamma \approx \Omega_m h e^{-\Omega_B(1+\Omega_m^{-1}(2h)^{1/2})}$. In earlier work a central value of $\sigma_8 \Omega_m^{0.56} = 0.55$ was used together with $\Gamma_{\text{eff}} = 0.22^{+0.07,+0.08}_{-0.04,-0.07}$. The old Γ prior is compared with the current version in Fig. 6. The change makes very little difference to parameter values obtained.

The original σ_8 prior choice was motivated by fits to the cluster temperature distribution, as was the decision to lower the central value by 15% made here. However, the philosophy we have adopted is to make the distribution broad enough so that reasonable uncertainties are allowed for in the prior. For example, there are many models that do not fit the shape as well as the amplitude of the cluster distribution. Thus the best σ_8 for a given model depends upon the temperature range chosen for the fit, and other physics might be involved. Especially with the reduced model spaces often considered, the formal statistical errors can look spectacularly good, but systematic issues undoubtedly dominate. Curiously, with the 15% drop, it seems like the σ_8 prior chosen could have been designed for the (weak) weak lensing results.

We will discuss the simulations in detail below, but we note here that the cases we have run

simulations on have $\sigma_8 = 0.9$ and 1.0 , and $\Gamma_{\text{eff}} = 0.18$ and 0.21 . The detailed baryonic dependence of the transfer function was included in the 0.18 case. The parameter choices were $\omega_b = 0.022$ and 0.0245 , $h = 0.7$, $\Omega_m = 0.3$ and 0.37 . A best-fit model to the data for many prior choices has $\omega_b = 0.02$, $\omega_c = 0.12$, $n_s = 0.95$, $\tau_C = 0$, and $\Omega_\Lambda = 0.7$ and with $h = 0.68$, $\Omega_b = 0.043$, $\Omega_{\text{cdm}} = 0.257$ with a 13.8 Gyr age; the normalization is $\sigma_8 = 0.76$, and $\Gamma = 0.18$ with $\Gamma_{\text{eff}} = 0.15$.

In general, CMB data provide weak constraints on the normalization of the matter fluctuations due to the added effects of the spectral tilt n_s and the optical depth parameter τ_C on the overall amplitude of the CMB power spectrum. Allowing for tensor modes in the power spectrum introduces further degeneracies. As shown in Paper V when fitting for a given parameter we adopt the conservative, and more computationally intensive, approach of marginalizing over all other variables considered.

In Table 2 we summarize the constraints on the LSS parameters from all available CMB data and a combination of priors. The mean and quoted (1σ) errors correspond to the 50% , 16% and 84% integrals of the marginalized likelihoods respectively. To explore the dependence of these values on the choice of data we also reproduce the table for a subset of CMB data which includes only CBI, DASI, BOOMERANG and *COBE*–DMR (Table 3). We see some sensitivity to the choice of data sets with the values of σ_8 lowered by the latter subset.

Correlations with τ_C are nontrivial, and allowing the space to be open in τ_C does tend to give higher marginalized σ_8 . In principle one could adopt a theory of early star formation when the smallest objects in the universe form to generate ionizing radiation, followed by overlap of the HII regions they create to build τ_C . This is tied to the growth of fluctuations, so a reasonable estimate might even be made. However such a τ_C prior is complex because it is tied to baryon density, mass collapse factor, massive star formation efficiency, amplifying radii for HII overlap, which is in itself dependent on breakout of the local density environment in which the stars form. Although it is fraught with sufficient uncertainty, as an illustrative exercise, we show what happens if the prior is a lognormal in τ_C with mean $\tau_{C*}=0.1$ and Gaussian width $\delta \ln \tau_C = \ln 2$. As expected from Fig. 9 we see the result is not huge, but a tighter restriction would shift σ_8 downward more. In Figs. 7 and 8 we also show the correlation of σ_8 and $\sigma_8 \Omega_m^{0.56}$ to other parameters considered.

It is also instructive to note that the best-fit models in all prior combinations select lower σ_8 models than the marginalized values. Typical best-fit models are: ($\Omega_{\text{cdm}} = 0.47$, $\Omega_\Lambda = 0.50$, $\Omega_b = 0.05$, $h = 0.51$, $n_s = 0.95$, $\tau_C = 0$ and $\sigma_8 = 0.73$) for both the weak prior and no prior cases; ($\Omega_{\text{cdm}} = 0.26$, $\Omega_\Lambda = 0.70$, $\Omega_b = 0.04$, $h = 0.68$, $n_s = 0.98$, $\tau_C = 0$ and $\sigma_8 = 0.78$) for flat, strong- h and LSS priors. This value of σ_8 is lower because the best-fits selected the $\tau_C = 0$ peak in the likelihood whereas integration over the relatively broad τ_C likelihood allows for the inclusion of high- σ_8 models.

Comparison of our results with independent estimates of σ_8 from CMB data is complicated by the different choices of parameter marginalization and by different treatments of the CMB data. Lahav et al. (2002) have carried out a joint CMB–2dF analysis of cosmological parameters. Their

result is $\sigma_8 = 0.73 \pm 0.05$ after marginalizing over some variables but keeping τ_C fixed at 0 and n_s fixed at unity. These values seem to agree with our best fit models which preferentially select $\tau_C = 0$ cosmologies. Lahav et al. (2002) also show how letting τ_C vary gives higher values for σ_8 . Melchiorri & Silk (2002) quote smaller values for σ_8 in their analysis. Although they usually fix τ_C to 0, even when τ_C is allowed to vary they get smaller results than those obtained here.

4. The Angular Power Spectrum of the Sunyaev-Zeldovich Effect

The SZ effect is a signature of the scattering of CMB photons off hot electrons. The effect can be described in terms of the fractional energy gain per scatter along the line of sight. By multiplying by the number density of electrons and integrating along the line of sight we can derive the induced temperature change about the mean:

$$\frac{\Delta T_{\text{SZ}}}{T_{\text{CMB}}} = -2y \psi_K(x) = -2\sigma_T \int n_e \frac{k_B(T_e - T_{\text{CMB}})}{m_e c^2} d\chi \psi_K(x), \quad (5)$$

where y is the Compton y -parameter, σ_T is the Thomson cross-section, n_e is the electron number density, T_e is the electron temperature, T_{CMB} is the CMB temperature, k_B is Boltzmann's constant and $m_e c^2$ is the electron's rest mass energy. Here $\psi_K(x)$, $x \equiv h\nu/k_B T_{\text{CMB}}$ is a frequency-dependent function which is unity at Rayleigh-Jeans wavelengths and is 0.975 at the 30 GHz frequencies probed by the CBI.

With the great increase in experimental sensitivity, measurement of the SZE in known clusters has become almost routine (see, e.g., Birkinshaw, Gull & Hardebeck 1984; Carlstrom et al. 1996; Holzapfel et al. 1997; Mason, Myers, & Readhead 2001; Udomprasert, Mason & Readhead 2001; Grainge et al. 2002). Coupled with X-ray observations of the cluster these measurements yield independent constraints on the value of the Hubble constant. They also provide a direct measurement of the amount of baryon mass in the cluster gas. The SZ effect is expected to contribute significantly to the CMB power spectrum at scales $\ell > 2000$, with a crossover point between the primary CMB and SZ signature occurring somewhere between $\ell \sim 2000$ and $\ell \sim 3000$. Surveys observing at these scales will therefore require accurate component separation to reconstruct the primary CMB spectrum and much work has focused on the issue of component separation in recent years. Many proposed experiments will adopt multi-frequency observing strategies in order to separate the different components by their different spectral dependence. These techniques cannot be applied to the narrow frequency band of the CBI observations. However we can attempt to address the question of whether the SZ effect could provide a contribution with the required amplitude to explain the observed excess.

We use the output of two separate hydrodynamical simulation algorithms in an attempt to predict the level at which the SZ effect will contribute to the CBI deep field observations. We also relate our numerical results to analytical models of the SZ power spectrum based on the halo model to test sensitivities to variations.

4.1. Hydrodynamical Simulations of the Sunyaev-Zeldovich Effect

The two codes we have employed both provide high-resolution dark matter and hydrodynamical simulations of large scale cosmic structure which we use to generate simulated wide-field SZ maps. Both simulation algorithms and processing techniques were developed independently (Pen 1998a; Bond et al. 1998, 2001; Wadsley et al. 2002) and are based on two different numerical schemes for solving the self-gravitating, hydrodynamical equations of motion. High-resolution gasdynamical simulations of large enough volumes are still beyond current technological capabilities. Following an approach taken previously by other authors (e.g., Springel, White & Hernquist 2001), we create a pseudo-realization of the cosmic structure up to high redshifts from a single, medium-sized, high-resolution simulation by stacking randomly translated and rotated (or flipped) copies of the (evolving) periodic volume.

One set of SZ simulations was obtained using the GASOLINE code, an efficient implementation of the (Lagrangian) smooth particle hydrodynamics (SPH) method (Wadsley et al. 2002). This tree+SPH code uses a pure tree-based gravity solver and has spatially-adaptive time stepping. It has been parallelized on many architectures (MPI in this case) and shows excellent scalability. The results presented here are based on the analysis of three high resolution Λ CDM simulations: two 200 Mpc box computations, with 256^3 dark matter plus 256^3 gas particles, and one 400 Mpc box computation, with 512^3 dark and 512^3 gas particles, a very large number for SPH simulations. The calculations were adiabatic, in the sense that only shocks could inject entropy into the medium. Despite the different sizes, all three simulations were therefore run with the same mass resolution. All simulations were run with a gravitational softening of 50 kpc (physical). The scale probed by the SPH smoothing kernel was not allowed to become smaller than the gravitational softening in the 200 Mpc runs, but it was not limited in the 400 Mpc run, which attained gas resolution scales as low as 5 kpc in the highest density environments, though increasing considerably at lower density. (64 neighbours were required to be within the smoothing kernel in the 400 Mpc run.) The 512^3 simulation was performed on a large-memory, 114 (667 MHz) processor SHARCNET COMPAQ SC cluster at McMaster University. It required about 80 GB of memory and took ~ 40 days of wall time to run. A detailed description of the 512^3 SPH simulation will be given in Wadsley et al. (2002).

Another set of SZ maps was obtained using a 512^3 run of the Moving Mesh Hydrodynamics (MMH) code of Pen (1998a). This code features a full curvilinear Total-Variation-Diminishing (TVD) hydro code with a curvilinear particle mesh (PM) N-body code on a moving coordinate system. We follow the mass field such that the mass per unit grid cell remains approximately constant. This gives all the dynamic range advantages of SPH simulations combined with the speed and high resolution of grid algorithms. The box size was 143 Mpc and the smallest grid spacing was 57 kpc (comoving). This 512^3 simulation used 30 GB memory and took about three weeks (~ 1500 steps) on a 32 processor shared memory Alpha GS320 using Open MP parallelization directives. The calculations were adiabatic as well.

The simulation boxes yield a number of projections of the gas distributions in random orientations and directions. The projections are then stacked to create a redshift range appropriate for the SZ simulation. In the case of the MMH simulation the angular size of the simulated box above a redshift of $z = 1.6$ is smaller than 2 degrees, the required angular size of the SZ simulations. To include the contributions from higher redshifts we tiled two copies of the periodic box to cover the increased angles. This only affects the smallest scales. All the maps were obtained with a low redshift cutoff at $z = 0.2$ to minimize the contribution from the closest clusters in the projections. The computational costs of running such large hydrodynamical simulations prevented us from obtaining targeted simulations with identical cosmological parameters from both algorithms at the time of writing. Below we account for the parameter variations in the models run when comparing the two simulations and we see a remarkable consistency between the results. The parameter variations are, in fact, an advantage for us since they provide us with a sampling of the SZE amplitude for processing through the CBI pipeline. We summarize the parameters used in the simulations in Table 1. We will report elsewhere the results of a detailed comparison of the two simulations with identical cosmological models and initial conditions.

The two 200 Mpc SPH simulations were used to generate 20 2x2 degree maps each while the MMH simulation yielded 40 separate maps. A detailed analysis of the MMH maps including SZ statistics and non-Gaussianity is given by Zhang, Pen & Wang (2002). A preliminary analysis of simulated SZ maps based on one of the 256^3 SPH simulations was presented by Bond et al. (2001), and a more detailed analysis will be presented elsewhere.

4.2. Hydrodynamical Simulation Results

In Fig. 10 we show the results for the $\sigma_8 = 1.0$, 143 Mpc MMH simulation, the $\sigma_8 = 1.0$ and 0.9, 200 Mpc SPH simulation and $\sigma_8 = 1.0$, 400 Mpc SPH simulation. The curves show averages for the \mathcal{C}_ℓ spectra from the 40 and 20 MMH and SPH maps respectively. The shaded regions show the full excursion of the power spectra in each set of maps. This gives a partial indication of the scatter induced in the power due to the small areas being considered. We compare these with a best-fit model to the BOOMERANG, CBI, *COBE*-DMR, DASI and MAXIMA data and an optimal combination of the mosaic and deep CBI, BOOMERANG, *COBE*-DMR, DASI and MAXIMA band powers (Paper V). The combined spectrum is designed for optimal coverage with variable bandwidths over the range of scales considered. At scales above $\ell \sim 1000$ the optimal spectrum is dominated by the contributions of the CBI mosaic and deep results.

To compare the cosmological simulations we have to account for the difference in parameters the simulations were run with. The dominant effect for the SZ \mathcal{C}_ℓ spectrum are variations in $\omega_b \equiv \Omega_b h^2$ and σ_8 , although differences in Ω_m and shape of the power spectrum will also have an influence. We have explored the σ_8 dependence of the SZ spectra in our numerical results. The top panel of Fig. 10 shows that the scaling $\mathcal{C}_\ell \propto \sigma_8^7$ brings the 200Mpc SPH run at $\sigma_8 = 0.9$ into essentially perfect alignment with the $\sigma_8 = 1$ run (yellow/square points). (Apart for the amplitude

the initial conditions in the simulations were the same). The exact factor n in a scaling of form $\mathcal{C}_\ell \sim \omega_b^2 \sigma_8^n$ depends upon the model in question, but $6 \lesssim n \lesssim 9$ is typical (Zhang, Pen & Wang 2002).

For the two separate σ_8 cases employed in the runs we rescale the spectra to a nominal $\omega_b = 0.022$, a value suggested by the CMB data. This enables us to compare the MMH result with the SPH results for the $\sigma_8 = 1$ runs (top panel Fig. 10). We see that the two codes give similar amplitudes over the range considered. In particular the two codes seem to give very close predictions for the contribution to the scales of interest for the CBI deep field result (green/hatched box). At larger angular scales the MMH simulation shows a somewhat higher amplitude than the SPH simulation. This may be in part due to the presence of a large rare cluster in the MMH volume simulation. The Poisson noise contribution of the large cluster is aggravated by the resampling technique adopted in the SZ map making stage described above. Variable redshift cutoffs do indeed confirm the dominant effect of this single cluster on the low- ℓ tail of the spectrum.

At smaller angular scales the two results start to diverge. The differences in spectral shape and cosmological parameters should not account for this. It may be attributable to the different techniques used to limit the resolution achievable, but this needs more investigation.

In the middle panel we have plotted the results from the 400 Mpc and 200Mpc SPH simulations which were both run with $\sigma_8 = 0.9$. We also compare this run to SZ power spectra derived from the 200 Mpc box SPH simulations of Springel, White & Hernquist (2001). The cosmological parameters of the Springel, White & Hernquist (2001) simulations were the same as those used in our SPH runs except for a value of $\omega_b = 0.018$. We also rescale this spectrum to the nominal $\omega_b = 0.022$. The agreement is remarkable.

We can contrast this level of agreement with the situation described in Springel, White & Hernquist (2001) where it appeared that different codes were giving quite different results. Nonetheless we plan a further exploration of the effects of lattice size variations and other numerical parameters to compare more exactly the MMH and SPH codes.

Based on these results we can calibrate the expected power to compare with the wide band result of Paper II

$$\begin{aligned} \text{SPH: } \mathcal{C}_\ell^{SZ} &\sim 170 \mu k^2 \frac{\omega_b^2}{(0.022)^2} \sigma_8^7 \\ \text{MMH: } \mathcal{C}_\ell^{SZ} &\sim 210 \mu k^2 \frac{\omega_b^2}{(0.022)^2} \sigma_8^7. \end{aligned} \quad (6)$$

For the CBI joint analysis of the three deep fields these amplitudes are at signal-to-noise ratios of approximately 0.4 for $\omega_b = 0.022$ and $\sigma_8 = 1.0$.

4.3. Analytic Modeling of the Sunyaev-Zeldovich Power Spectrum

The general analytic framework comes under the generic name of “halo models”, in which simple parameterized gas profiles within clusters and groups are constructed, appropriately scaled according to the masses. The gas profile in a halo and halo mass-temperature relation determines the SZ effect of the halo. The abundance of the halos as a function of mass and redshift is determined by the Press & Schechter (1974) formula, the peak-patch formula, or formulas derived from fits to N -body simulations. Clustering of the halos is included through simple linear biasing models. The halo model approach has been applied to the SZ effect by many authors over time (e.g., Bond 1988; Cole & Kaiser 1988; Makino & Suto 1993; Bond & Myers 1996; Atrio-Barandela & Mucket 1999; Komatsu & Kitayama 1999; Cooray 2000; Molnar & Birkinshaw 2000; Seljak, Burwell & Pen 2001). There has still not been an adequate calibration of the relation between the physical parameters describing the gas distribution in the halos and the results of gas dynamical simulations, and usually the parameters that have been adopted are those derived from observations of clusters at low redshift. We show here that we can get reasonable fits to our simulation results by choosing suitable gas profile parameters. However we caution that the gas profile is a function of halo mass and redshift, so globally fitting to our “observed” SZ power spectrum may not deliver reliable parameters for the analytic model. However, in the simulations we can measure the gas profile parameters and then apply the halo models to calculate the SZ power spectrum, as we address in our SZ comparison project. For now, we take our globally fit models to show sensitivity to parameter variations.

In the bottom panel of Fig. 10 a few analytic models are shown to compare with the $\sigma_8 = 1$ MMH simulation. For the halo comoving number density n as a function of halo mass M and redshift z : $Mdn/dM \propto (2/\pi)^{1/2} (\bar{\rho}_0/M) |d \ln \sigma / d \ln M| \nu e^{-\nu^2/2}$, where $\nu \equiv (\delta_c/\sigma)$, the Press-Schechter distribution. Here $\bar{\rho}_0$ is the present mean matter density of the universe. $\sigma(M, z)$ is the linear theory *rms* density fluctuation in a sphere containing mass M at redshift z . It is calculated using the input linear density power spectrum $P(k)$ of our simulations, which is truncated at $k_{\text{lower}} = 2\pi/L$ and $k_{\text{upper}} = \sqrt{3}\pi N/L$ due to the finite box size L and resolution N of simulations, respectively. In this formula, we have taken $\delta_c = 1.686$ as the linearly extrapolated spherical overdensity at which an object virializes. Although this is strictly valid only for $\Omega_{\text{tot}} = 1$ cosmologies, when Ω_m decreases from 1 to 0.3, δ_c only decreases from 1.686 to ~ 1.675 (Eke et al. 1996). We omit this dependence of δ_c on Ω_m , Ω_Λ and therefore redshift, for the $\Omega_m = 0.37$ Λ CDM we are trying to fit here. We also truncate the mass integral at a specified lower mass limit M_{lower} , which we choose as a free parameter. In these analytic estimates, clustering is usually treated with simple linear models in which the long wavelength cluster distribution is amplified over the underlying mass distribution by a mass-dependent biasing factor, leading to a power spectrum $b(M_1)b(M_2)P(k)$ amplified over the underlying dark matter spectrum $P(k)$. This turns out to be a small effect for the SZ power spectra.

To describe the gas profile, we need the pressure profile. We take this to be that for an isothermal distribution with a baryon density profile given by a β model with $\beta = 2/3$. For the gas

temperature, we adopt the virial theorem relation given in Pen (1998b): $M/M_8 = (T/T_8)^{3/2}$, where M_8 is the mean mass contained in an $8h^{-1}\text{Mpc}$ sphere and $T_8 = 4.9\Omega_m^{2/3}\Omega(z)^{0.283}(1+z)\text{keV}$. $\Omega(z)$ is the fraction of matter density with respect to the critical density at redshift z . This relation was obtained by comparing the gas temperature distribution in simulations with the halo mass function described above. For the electron number density profile we adopt $n_e = n_{e0} [1 + r^2/r_{\text{core}}^2]^{-1}$, scaled by the central density n_{e0} and core radius r_{core} . Since our simulations show that the pressure profile falls off more rapidly than the product of temperature and density given here would indicate, we truncate the pressure at a fraction fr_{vir} of the “virialized radius” r_{vir} . The virial radius is defined as the radius of a sphere with mass M and mean density $\Delta_c(z)\bar{\rho}(z)$, where $\bar{\rho}(z)$ is the mean matter density at redshift z and Δ_c is given by Eke et al. (1996). If we assume that gas accounts for a fraction Ω_B/Ω_m of the halo mass, the baryon content fixes one of the 3 parameters, n_{e0} . We treat f and $r_{\text{vir}}/r_{\text{core}}$ as free parameters to be fit to the SZ power spectrum.

The bottom panel of Fig. 10 shows typical fits we can obtain with the above model using $r_{\text{vir}}/r_{\text{core}} = 4.8$ and $f = 0.9$. Given the number of free parameters, many combinations of values can yield reasonable fits. In order to investigate the resolution effects in our simulations we fix r_{vir}/r_c and f and vary the lower mass cutoff M_{lower} and the k range cutoff in the analytic model. These parameters are related to the resolution limitations of our simulations. For the MMH simulation, we find the effect of the k range cutoff is negligible, but that M_{lower} has a larger effect. Since we need more than 100 gas and dark matter particles to resolve a halo, we choose M_{lower} as the mass of 100 gas particles and 100 dark matter particles. This corresponds to $0.0015M_8$ for the 512^3 simulation. We see substantial deviations developing when $M_{\text{lower}} > 0.01M_8$. There are as well other uncertainties not included in our hydro simulations, which are adiabatic. For example, the outflow of gas from groups could lead to an effective mass cutoff that is physical rather than resolution dependent. The concentration parameter for gas, $r_{\text{vir}}/r_{\text{core}}$ could be a function of mass and of redshift, which would also change the results.

5. Simulating CBI Observations of the Sunyaev-Zeldovich Effect

The estimation of band powers used in the analysis of the CBI observation is based on a maximum likelihood technique which assumes the signal to be a Gaussian random field (Paper IV). This assumption appears to be justified in the case of primary CMB anisotropies where no clear evidence of non-Gaussianity has been found. However, the contributions from various foregrounds are non-Gaussian. Although the observations are noise dominated at the scales of interest for the CBI deep field excess and therefore expected to be predominantly Gaussian, it is important to test the effect of a small non-Gaussian signal such as a SZ foreground on the band power estimation procedure.

We used the simulated SZ maps to test the effect of a SZ foreground on the CBI analysis pipeline. To do this we construct detailed mock data sets using the CBI simulation tools (Paper IV). We take real observations for particular dish configurations and pointings and replace the observed

visibilities by realizations of the expected signal and instrumental noise. This results in simulated observations with identical uv coverage as the actual observations. The simulations can also include foreground templates as a distribution of point sources or maps of the SZE.

Each simulated 2×2 degree SZE map is used as a foreground and added to a primary CMB background to generate mock observations of the 08^h deep field. One point to note is that the CBI observations are actually differenced to minimize any ground pick-up (Paper II). This involves subtracting the signal from two fields (*lead* and *trail*) separated by 8 minutes of right ascension on the sky. In adding a SZE foreground to the simulated observations two separate SZE maps were used as *lead* and *trail* fields. For this exercise we create 20 simulated observations using the 40 MMH maps and 10 for the 20 SPH maps.

The mock data sets were then processed through our power spectrum estimation pipeline described in Paper IV. The maximum likelihood calculation of the power spectrum uses template correlations to project out the expected contribution from point source foregrounds. Since point source templates are projected out of the data or constrained at a known amplitude (as in the case of the residual unresolved background) the power in the excess is assigned to the CMB when fitting for the band powers since no other correlations are included in the quadratic power spectrum estimator (except for instrumental noise). We reproduce this situation by simulating observations of primary CMB realizations with SZE foregrounds but only allowing for noise and CMB contributions to the total correlation matrix in the likelihood

$$\mathbf{C} = \mathbf{C}^N + \mathbf{C}^{\text{CMB}}, \quad (7)$$

where the correlations due to the CMB are expressed as a function of the band powers C_B with

$$\mathbf{C}^{\text{CMB}} = \sum_B C_B \frac{\partial \mathbf{C}^{\text{CMB}}}{\partial C_B}. \quad (8)$$

The SZE maps were produced from simulations of different cosmologies and we have shown how the spectra can be scaled to fiducial ω_b and σ_8 values for comparison. However when simulating the measurement of band powers we choose to use unscaled contributions in order to test the different amplitude regimes given by the different values of baryon density. As a primary CMB signal we use random realizations of a single Λ CDM model ($\Omega_m = 0.30$, $\Omega_b = 0.04$, $\Omega_\Lambda = 0.70$, $h = 0.68$ and $n_s = 0.975$). For the SZE contributions we restrict ourselves to the $\sigma_8 = 1.0$ simulations.

Results are shown in Fig. 11. The band powers are averaged over the 20 and 10 independent realizations from the two $\sigma_8 = 1.0$ simulations. The triangles (red) are for the MMH simulations and the SPH results are shown as squares (blue) points. The model used for the primary CMB contribution is also shown together with the 2σ confidence region for the deep excess. The errors shown are obtained from the variance of the measured band powers. The averages appear to recover the input power accurately in both regimes where either the primary CMB signal or SZE signal dominate.

The interpretation of the errors is of course complicated in the SZ dominated regime by the non-Gaussianity of the SZ signal (eg. Zhang, Pen & Wang 2002). The small area considered in the simulations results in significant sample variance effects in the measurements of the SZ power. The scatter in the observed band powers over the different realizations is also shown in Fig. 11. The non-Gaussian scatter is significant although this effect would decrease for the larger area probed by the joint, three field analysis and the high- ℓ errors are dominated by the noise. It is also important to note that if the SZE is a significant source of the power in the observations, the sample variance component of the errors derived in the optimal spectrum estimation would be biased.

It is also interesting to note the effect of the low- ℓ contribution in the MMH simulations. There is a sizable contribution to the band powers below $\ell \sim 2000$. Although this effect may be due to the presence of a rare sized cluster in the simulation as discussed above it raises the question of whether a SZ signal with high enough amplitude to explain the excess may already be constrained by its low- ℓ contributions.

6. Sunyaev-Zeldovich Filtering of the CBI Deep Field Observations

In § 2 we discussed the filtering of the CBI deep fields as a method of component separation. Using the specific SZ models we introduced above we can now extend the image analysis by template filtering the images specifically for SZ contributions.

As a check we start by creating mock observations of the 2×2 degree deep fields containing only SZ foregrounds and noise. We then filter the images with the average SZ spectra of the simulations. This of course does not account for the correlations in a non-Gaussian component such as the SZ foreground. As described in the previous section, only CMB, instrumental noise and point sources are accounted for in the total correlation matrix assumed for the data. The template is therefore constructed as

$$\mathbf{C}^{\text{SZ}} = \sum_B C_B^{\text{SZ}} \frac{\partial \mathbf{C}^{\text{CMB}}}{\partial C_B}. \quad (9)$$

where the amplitudes C_B^{SZ} are obtained by filtering the average SZ power spectra by the deep field band window functions (see Paper II).

The resulting images should reproduce the structure in the input SZ maps and we find that this is indeed the case. The sequence of images in Fig. 12 is an example of the filtering for one of the SPH maps (top row) and one of the MMH maps (bottom row). The left most images are the input SZ maps (*lead-trail*). The middle images show the result of filtering mock data sets where the noise has been reduced to negligible levels. These essentially noise-free mocks provide a control to compare to the reconstructed noisy observations shown on the right. The strongest features in both images reproduce the strongest SZ signatures in the input templates, although one has to take into account the tapering effect induced by the primary beam when comparing the input maps to the filtered data (see Paper IV). The tapering suppresses the amplitude of significant features

further out in the beam with respect to those close to the centre of the field. The noise level is such that the significance of the “detections” is not obvious. These can be quantified by comparing with the allowed fluctuations about the mean Wiener filter (Eq. 4).

We have applied the same filtering to the deep field observations. In this case the primary CMB signal is a further source of noise. The nature of the Wiener filter is such that the power in the filtered image will scale linearly with the overall normalization of the SZ template. By calibrating the SZ template filters with the observed power in the deep high- ℓ result we can therefore obtain an image with the same signal-to-noise ratio of the observations. We have found a number of possible candidate features in the filtered data. These features also appear to be stationary when the data sets are split into roughly equal halves. The splits provide observations of the same signal under the assumption of independent noise and thus any significant correlations between the two can be attributed to the signal. As can be seen by the comparison between input and output maps in Fig 12, identifying single features in the images with actual objects in the field of view must be done cautiously. We are currently investigating the significance of the candidate features and this work will be reported elsewhere.

7. Discussion

We have presented estimates for the possible contribution from the SZ effect to the CBI deep field observations which show evidence of an excess in power over standard primary CMB scenarios above $\ell \sim 2000$. Our numerical simulations show that an amplitude of $\sigma_8 \approx 1$ appears to give, on average, enough power in the SZ signature to explain the excess. CMB and LSS data favour models with somewhat lower normalizations ($\sigma_8 = 0.87^{+0.15}_{-0.09}$ for flat, HST- h and LSS priors) even when taking very conservative priors on τ_C . Although it appears that $\sigma_8 \approx 0.9$ does not reproduce the anomaly, we caution that the sample variance of the SZE is large according to our simulations.

The excellent agreement among the runs using the two separate hydrodynamic algorithms is encouraging and lends support to the conclusions on the required normalization. We note that the simulations employed in this work were developed and run independently from each other and the CBI analysis effort (Bond et al. 2001; Zhang, Pen & Wang 2002). However, both simulations were adiabatic, with entropy increases occurring only by shock heating. The influence of cooling and entropy injection from supernovae, etc., on the predicted SZ spectrum remains to be explored, as does the effect of such technical issues as numerical convergence as the simulation resolution is changed.

The limited number of mock simulations we have carried out show that our experimental setup does reproduce correctly the signal of simulated SZ foregrounds. This suggests the Gaussian assumption implicit in our band power estimation procedures does not break down at the SZ signal-to-noise ratios of the deep field observations.

If the excess is not due to the SZE, what could it be? Other possible origins of the excess

were addressed in Paper II. It is inconsistent with adiabatic inflationary predictions for primary anisotropies on the damping tail only at the $\sim 3\sigma$ level. The excess clearly needs to be further explored, both within the CBI dataset itself, and also by correlating with other observations of these deep fields. The Wiener filter technique of § 2 and § 6 is promising for the identification of robust features in the CBI data to aid in the follow-up observations, given a model power spectrum to use in the filters.

Our principal conclusion is that the CBI anomaly could be a result of the SZ effect for the class of Λ CDM concordance models if σ_8 is in the upper range of values allowed by current CMB data. The simple $\mathcal{C}_\ell \propto \sigma_8^7 \omega_b^2$ scaling that we have found from our simulations (eq. 6) shows that the lower σ_8 values preferred by the CMB data imply SZ signals below, but not too far below, the sensitivity obtained by the CBI deep observations. This work also highlights how the signature of the SZ effect has great potential for constraining the amplitude σ_8 . The sensitive scaling of the CMB power with σ_8 will result in significant constraints even with large errors on the observed bandpowers. This further underlines the significance of “blank field” observations with interferometers at $\ell \gtrsim 2000$ which should reveal the SZ structure that necessarily lurks as a byproduct of CMB-normalized structure formation models.

We thank Hugh Couchman, Tom Quinn and Joachim Stadel for interactions on the computational issues. Research in Canada is supported by NSERC and the Canadian Institute for Advanced Research. The computational facilities (SHARCNET at McMaster and PSciNet at Toronto) are funded by the Canadian Fund for Innovation. This work was supported by the National Science Foundation under grants AST 94-13935, AST 98-02989, and AST 00-98734. We are grateful to CONICYT for granting permission to operate the CBI at the Chajnantor Scientific Preserve in Chile.

REFERENCES

Atrio-Barandela, F. & Mucket, J., 1999, ApJ, 515, 465

Bacon, D., Massey, R., Refregier, A., & Ellis, R. 2002, MNRAS, submitted (astro-ph/0203134)

Bardeen, J. M., Bond, J. R., Kaiser, N., & Szalay, A. S. 1986, ApJ, 304, 15

Bennett, C. L. et al. 1996, ApJ, 464, L1

Birkinshaw, M., Gull, S. F., Hardebeck, H. 1984, Nature, 309, 34

Bond, J. R. 1988, in *The Early Universe*, ed. W.G. Unruh (Reidel)

Bond, J. R. 1994, in Relativistic Cosmology, M. Sasaki, ed., Proc. 8th Nishinomiya-Yukawa Memorial Symposium (Academic Press) (astro-ph/9406075)

Bond, J. R. 1996, in Cosmology and Large Scale Structure, Les Houches Session LX, eds. R. Schaeffer et al. (Elsevier), p. 469

Bond, J. R. & Crittenden, R. G., 2002, in Structure Formation in the Universe, 241-280, R.G. Crittenden and N.G. Turok, eds., Proc. NATO ASI (Kluwer Academic Publishers) (astro-ph/0108204)

Bond, J. R. & Efstathiou, G. 1987, MNRAS, 226, 655

Bond, J. R. & Jaffe, A. H. 1999, Large-Scale Structure in the Universe, Philosophical Transactions of the Royal Society of London A, 1998

Bond, J. R., Kofman, L., Pogosyan, D. & Wadsley, J. in: Colombi, S. & Mellier, Y., ed., Wide Field Surveys in Cosmology, Proc. XIV IAP Colloquium

Bond, J. R. & Myers, S. 1996, ApJS, 103, 1

Bond, J. R., Ruetalo, M. I., Wadsley, J. W. & Gladders, M. D., 2001 (astro-ph/0112499)

Carlberg, R. G., Morris, S. L., Yee, H. K. C., Ellingson, E. 1997, ApJ, 479, L19

Carlstrom, J. E. et al. , 1996, ApJ, 456, L75

Cole, S. & Kaiser, N., 1988, MNRAS, 233, 637

Condon, J. J., Cotton, W.D., Greisen, E. W., Yin, Q. F., Perley, R. A., Taylor, G. B., & Broderick, J. J. 1998, AJ, 115, 169

Cooray, A., 2000, Phys. Rev. D, 62, 103506

Dodelson, S., 2002 (astro-ph/0107421)

Efstathiou, G., Bond, J. R. & White, S. D. M. 1992, MNRAS, 258, 1P

Eke, V. R., Cole, S., Frenk, C. S. 1996, MNRAS, 282, 263

Fan & Bahcall 1998, ApJ, 504, 1

Grainge, K., et al. 2002, MNRAS, 329, 890

Halverson, N. W. et al. 2002, ApJ, 568, 38

Holzapfel, W. L. et al. 1997, ApJ, 479, 17

Hoekstra, H., Yee, H. K. C. & Gladders, M. D. 2002 (astro-ph/0204295)

Jaffe, A. H., 1999, Phys. Rev. Lett., 86, 3475

Komatsu, E. & Kitayama, T., 1999, ApJ, 526, L1

Lahav, O., et al. 2002, MNRAS, in press (astro-ph/0112162)

Lang, A. E., et al. 2001, Phys. Rev. D, 63, 042001

Lee, A. T., et al. 2001, ApJ, 561, L1

Makino, N., & Suto, Y., 1993, ApJ, 405, 1

Mason, B. S., Myers, S. T., & Readhead, A. C. S. 2001, ApJ, 555, L11

Mason, B. S., et al. 2002, ApJ, submitted (Paper II)

Mauskopf, P. D., et al. 2000, ApJ, 536, L59

Melchiorri, A. & Silk, J., 2002 (astro-ph/0203200)

Miller, A. D., et al. 1999, ApJ, 524, L1

Mo, H. J. & White, D. M., 1996, MNRAS, 282, 347

Molnar, S. & Birkinshaw, 2000, ApJ, 537, 542

Myers, S. T. et al. 2002, ApJ, submitted (Paper IV)

Netterfield, C. B., et al. 2002, ApJ, in press (astro-ph/0104460)

Padin, S., et al. 2001, ApJ, 549, L1 (Paper I)

Peacock, J. A. & Dodds, S. J. 1994, MNRAS, 267, 1020

Peacock, J. A., et al. 2001, Nature, 410, 169

Pearson, T. J., et al. 2002, ApJ, submitted (Paper III)

Peebles, P. J. E. & Yu, J. T. 1970, ApJ, 162, 815

Pen, U.-L., 1998a, ApJS, 115, 19

Pen, U.-L., 1998b, ApJ, 498, 60

Pen, U.-L. 1998, ApJ, 504, 60

Pierpaoli, E., Scott, D., & White, M. 2001, MNRAS, 325, 77

Press, W. H. & Schechter, P. 1974, ApJ, 187, 425

Pryke, C., Halverson, N. W., Leitch, E. M., Kovac, J., Carlstrom, J. E., Holzapfel, W. L., & Dragovan, M. 2002, ApJ, 568, 46

Refregier, A., Rhodes, J., & Groth, E. J. 2002, ApJ, submitted (astro-ph/0203131)

Reiprich, T. H. & Böhringer, H. 2001 (astro-ph/0111285)

Szalay, A. S., et al. 2001 (astro-ph/0107419)

Seljak, U. 2001, MNRAS, submitted (astro-ph/0111362)

Seljak, U., Burwell, J. & Pen, U.-L., 2001, Phys. Rev. D, 63, 063001

Sievers, J. L., et al. 2002, ApJ, submitted (Paper V)

Silk, J. 1968, ApJ, 151, 459

Springel, V., White, M., & Hernquist, L. 2001, ApJ, 549, 681, erratum; Springel, V., White, M., & Hernquist, L. 2001, ApJ, 562, 1086

Sugiyama, N. 1995, ApJS. 100, 281

Sunyaev, R. A. & Zeldovich, Ya. B. 1970, Ap&SS, 7, 3

Verde, L. et al., MNRAS, submitted (astro-ph/0112161)

Viana, P. T .P., Nichol, R. C., Liddle, A. R. 2001, ApJ, submitted, (astro-ph/0111394)

Udomprasert, P. S., Mason, B. S., and Readhead, A. C. S. 2000, in Constructing the Universe with Clusters of Galaxies (IAP 2000 meeting, Paris), ed. F. Durret and D. Gerbal

Wadsley, J. W., Couchman, H. M. P, Stadel, J. & Quinn, T., in preparation

van Waerbeke, L., Mellier, Y., Pello, R., Pen, U.-L, McCracken, H. J., & Jain, B. 2002, A&A, submitted (astro-ph/0202503)

Zhang, P. J., & Pen, U.-L., 2001, ApJ, 549, 18

Zhang, P. J., Pen, U.-L. & Wang, B. 2002, ApJ, in press (astro-ph/0201375)

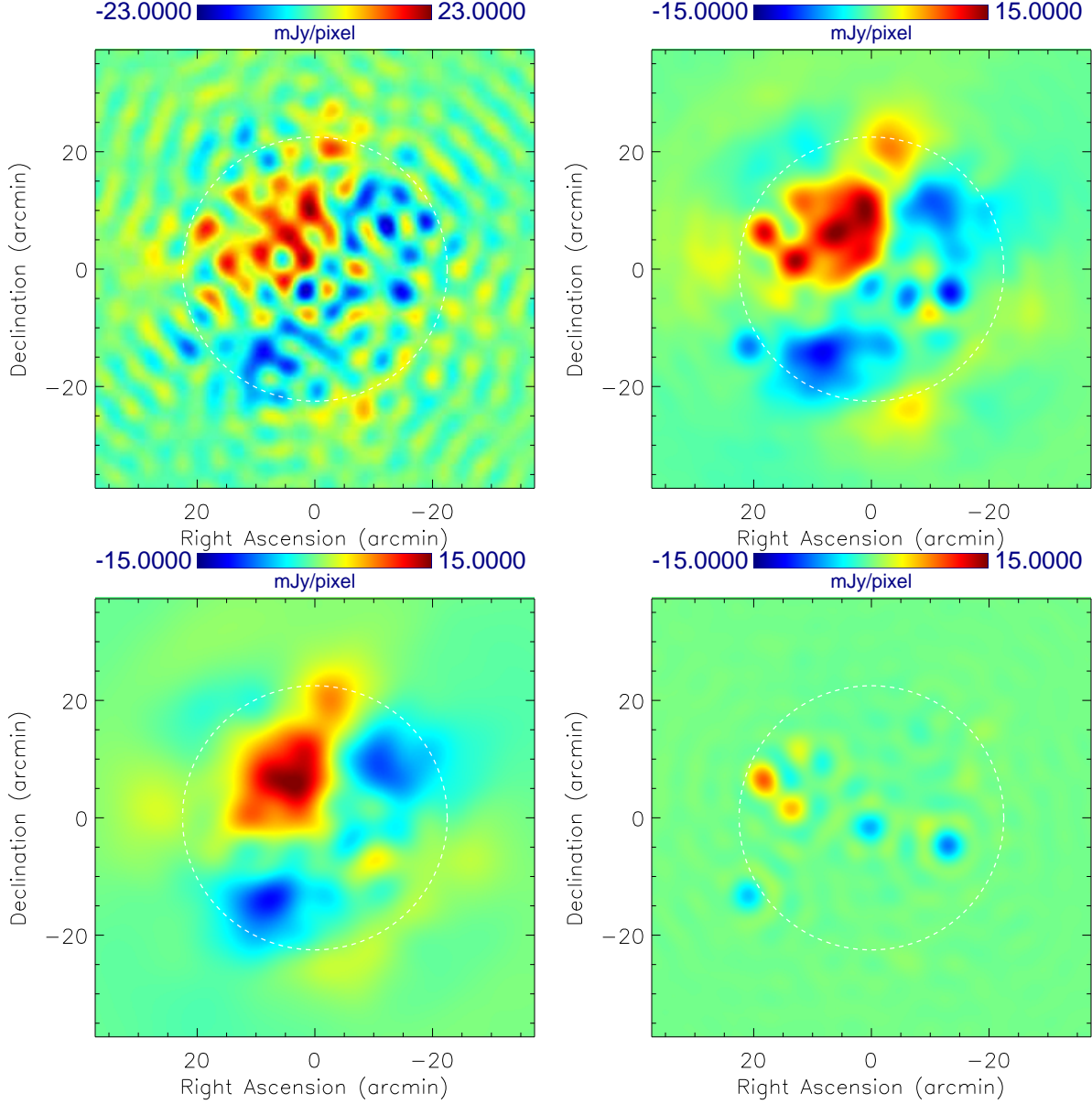


Fig. 1.— Filtered images of the CBI 08^h deep field. The total signal *plus* noise image (top left) displayed as a 70' by 70' field. The white (dashed) circle shows the 45' FWHM of the primary beam. A total signal image (top right) is obtained by using the sum of CMB and point source foreground correlations as a template. The amplitude of the residual source background is set to a flux of $0.08\text{Jy}^2\text{sr}^{-1}$ in the filter. Using the joint deep field band powers as amplitudes in the filters we obtain the optimal image for the CMB (bottom left). This image encompasses the power attributed to the high- ℓ excess. The known point source residuals can also be filtered out of the data (bottom right). Colour scales are kept constant for the filtered images to ease comparison of the relative amplitudes of the components. The images are deconvolved by the response of a simulated source placed at the centre of the field.

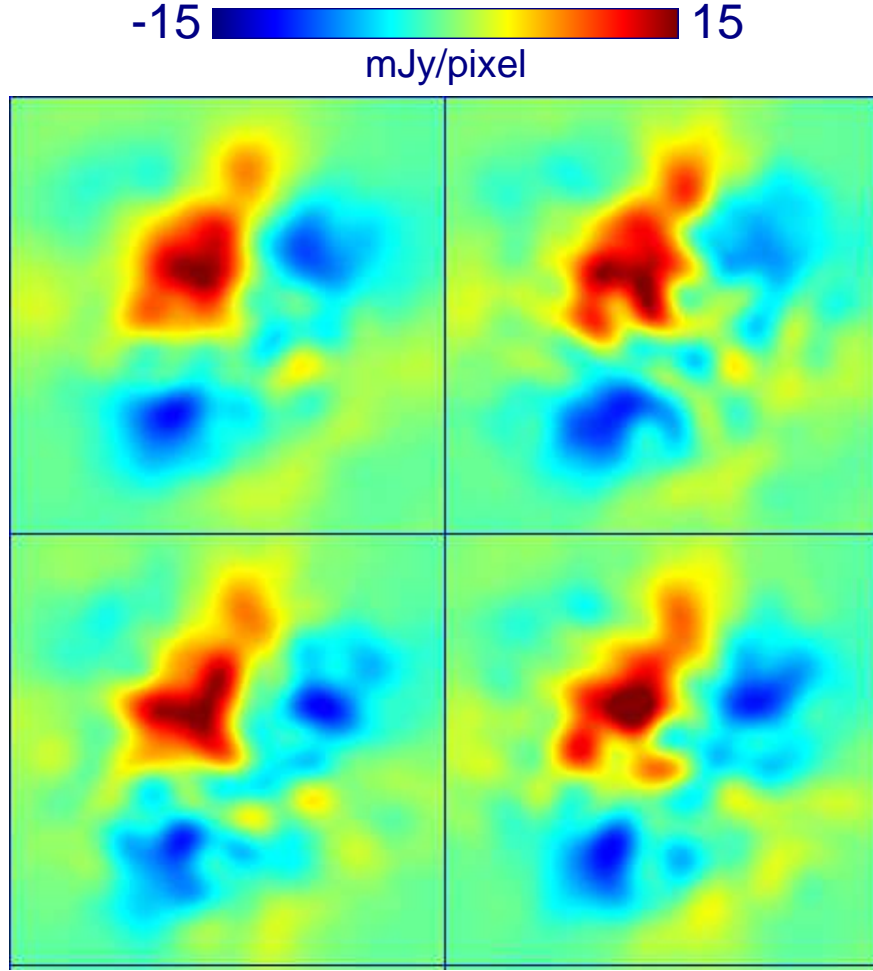


Fig. 2.— 08^h Wiener filtered map uncertainties. The top left panel reproduces the mean CMB component map of Fig. 1. The remaining three panels show the addition of three constrained realizations of the allowed fluctuations to the mean map. At the signal-to-noise ratios of the larger scale CMB observations the features are robust to the fluctuations. This gives a visual indication of the confidence one can draw from the features in the map.

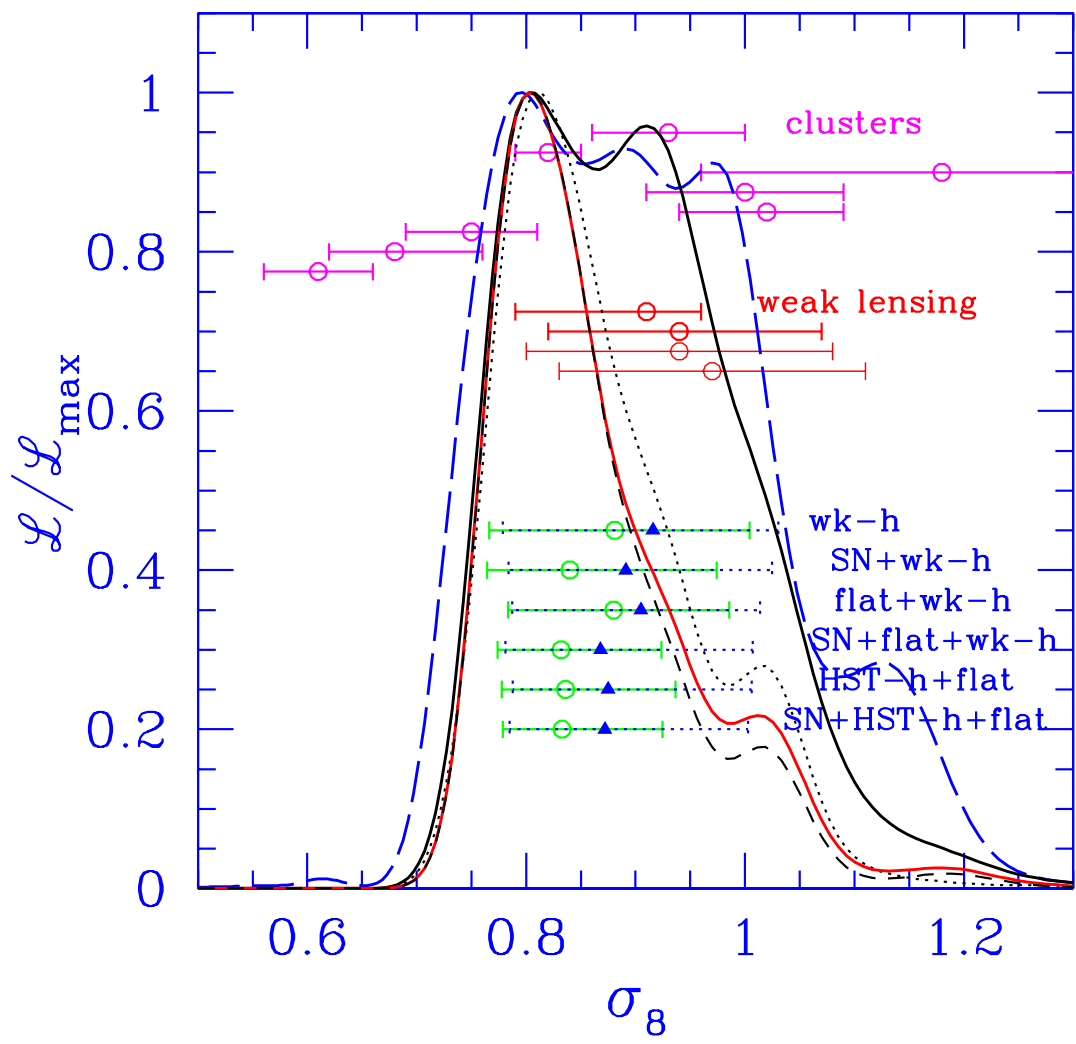


Fig. 3.— One-dimensional projected likelihood functions of σ_8 calculated for increasingly restrictive prior probabilities on the cosmological parameters are shown. The curves shown used DMR, DASI(Halverson et al. 2001), BOOMERANG(for the Netterfield et al. (2002) cut) and the CBI mosaic data for the odd $\Delta L=140$ binning. The marginalization has been performed over 6 cosmological variables and all of the relevant calibration and beam uncertainty variables associated with the experiments, four in this case. The weak- h prior is long-dashed blue, the flat weak- h prior is solid black and the flat strong- h (HST- h restriction) prior is shown in solid red. The action of the SN1a prior on the flat weak- h prior is shown as short-dashed black. Dotted black shows the action of the LSS prior. The Bayesian 50% and associated 16% and 84% error bars are shown in green for these and other prior combinations. Using MAXIMA (Lee et al. 2001), TOCO (Miller et al. 1999) and 17 other experiments predating April 1999 (hereafter “April 99”) as well gives similar results: the measurements shown as solid blue triangles with dotted blue error bars are for this choice of data. The original LSS prior was constructed based on the cluster abundance data (Bond 1996; Bond & Jaffe 1998; Lange et al. 2001). Estimates of σ_8 from cluster abundance data and recent estimates from weak lensing data are also shown. These results have invariably had more restrictive priors imposed, and so are not always applicable, but the overall level of agreement in the various approaches is encouraging.

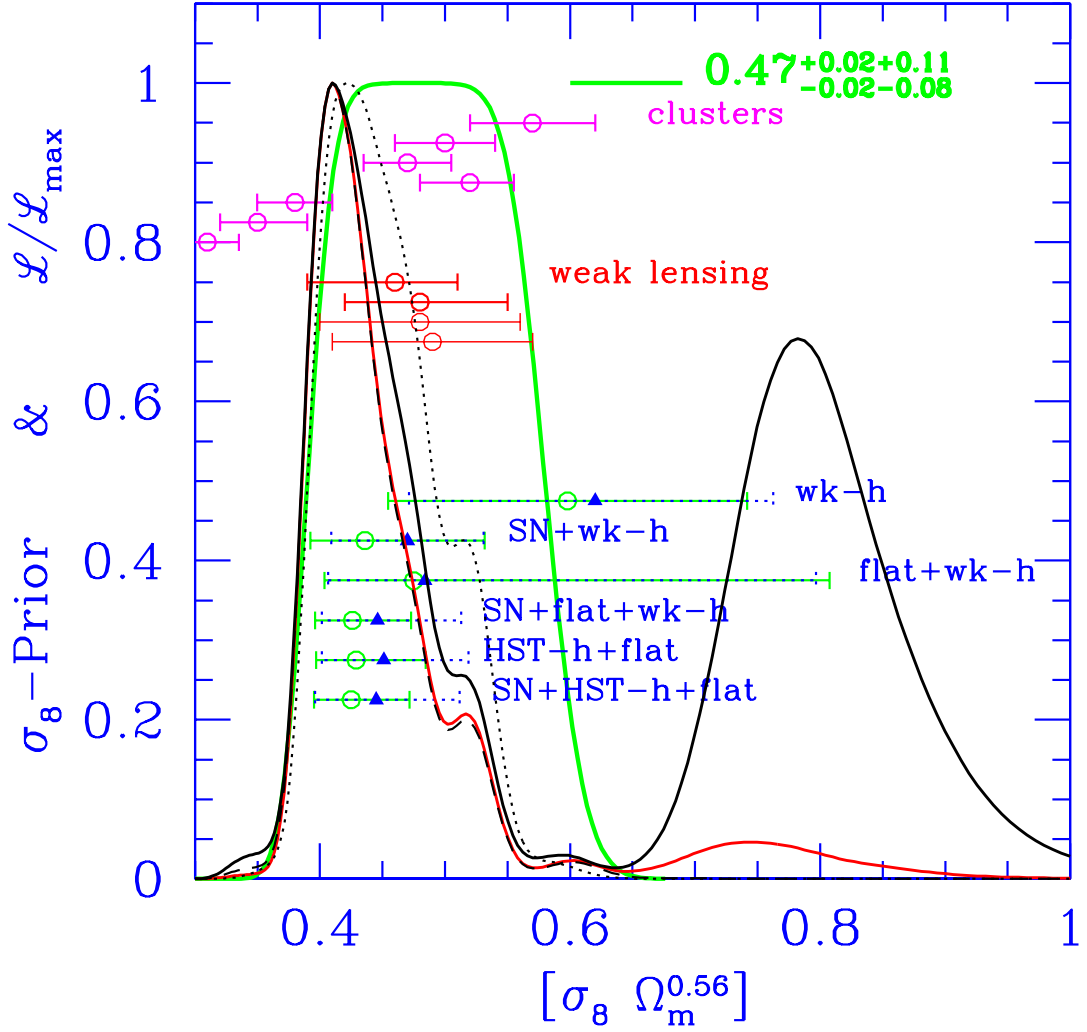


Fig. 4.— The weak prior for LSS in $\sigma_8 \Omega_m^{0.56}$ is compared with current data and the CMB plus non-LSS priors. The prior used in past work was shifted up in central value from 0.47 to 0.55, but was otherwise the same. Shown here are results for the DMR+DASI+BOOMERANG+CBI mosaic data. 1D projected likelihood functions for the restriction to $\Omega_{tot} = 1$ case are plotted. Note the double-humped solution, which largely disappears if either the SN1a constraint is imposed, or the $wk-h$ prior is strengthened to the $strong-h$ prior, the $HST-h$ constraint. If instead the weak LSS prior is included, it does almost the same thing.

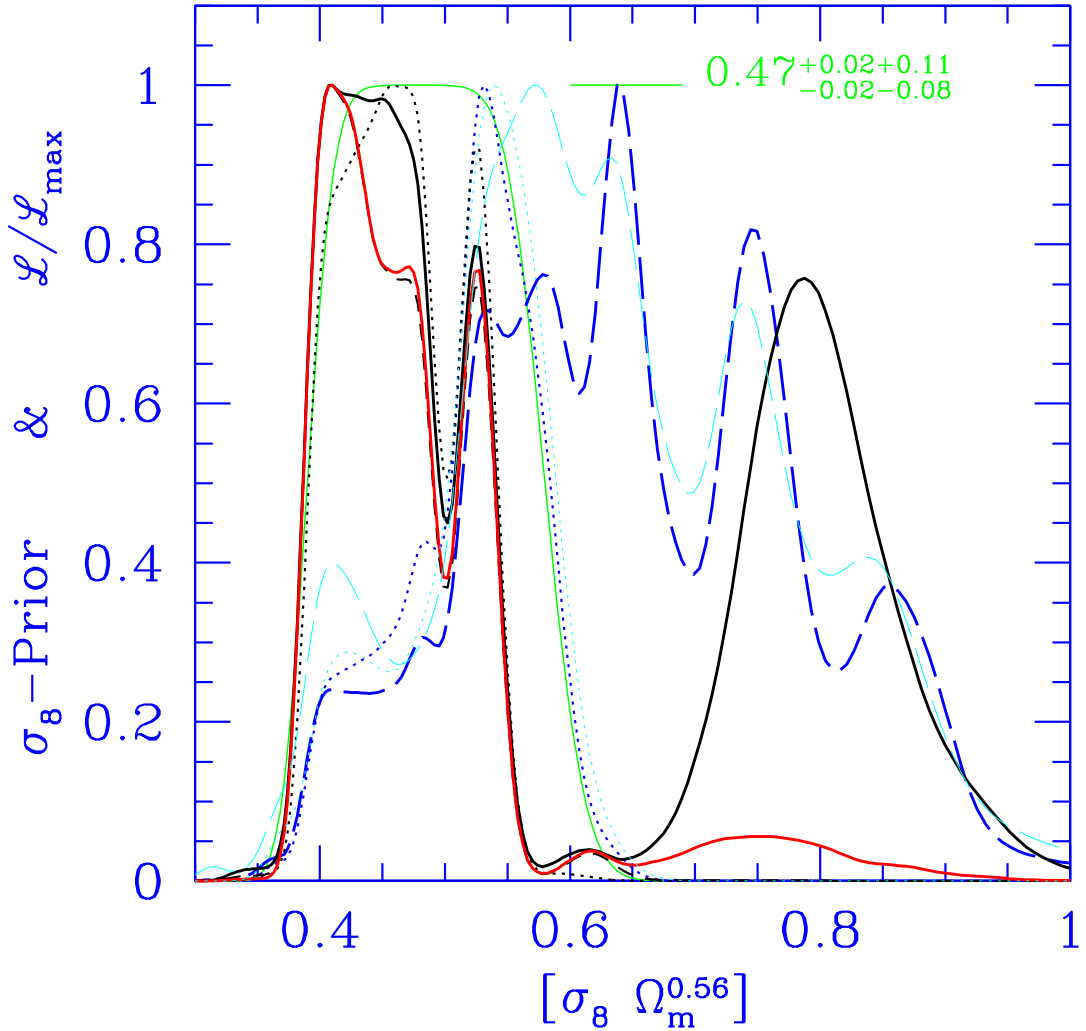


Fig. 5.— 1D projected likelihood functions calculated using all of the CMB data show explicitly the action of the LSS prior (dotted blue and black) upon the weak- h prior (long-dashed blue) and the flat weak- h prior (solid black). The action of the SN1a prior on the flat weak- h prior is shown in short-dashed black, and the flat strong- h prior is shown in solid red. The flat cases can be contrasted with those in Fig. 4 which show the same curves using only DASI+BOOMERANG+CBI+DMR. For the weak- h prior case, the light long-dashed cyan and dotted cyan use the DMR+DASI+BOOMERANG+CBI data, and should also be contrasted with the equivalent blue curves. The variation with data set is less strong in the σ_8 variable of Fig. 3. Note that the action of the LSS constraint on the weak- h prior is to concentrate it near in the edge of the allowed σ_8 regime, but that this is not the case when the flat constraint is added.

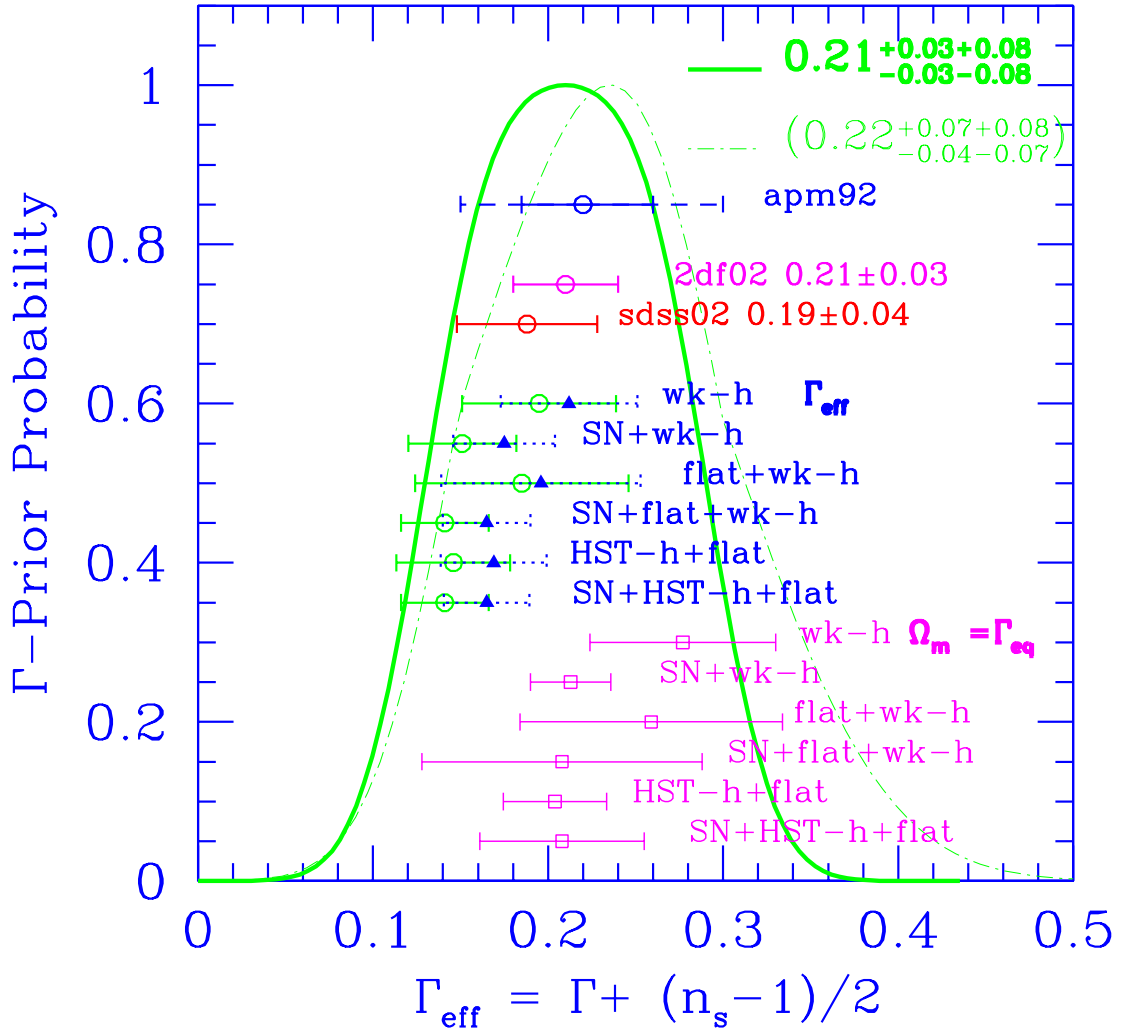


Fig. 6.— The prior probability used for the shape parameter Γ_{eff} is heavy green. (This is to be contrasted with the more skewed one used in Lange et al. (2001), etc., shown as light dashed-dotted green.) The Γ -prior was designed to encompass the range indicated by the APM data, vintage 1992, but new estimates from 2dF and SDSS surveys shown below are quite compatible. The CMB results for Γ_{eff} are shown with various choices for priors for comparison. Solid green is DMR+DASI+BOOMERANG+CBI. Γ_{eff} includes corrections for ω_b , h , and the tilt, and since the tilt depends slightly upon which data sets are used, the dotted blue results for MAXIMA, TOCO, BOOMERANG-NA (Mauskopf et al. 2000, hereafter B97) and 17 other experiments as well are also shown. The related values of $\Omega_m h$ shown in magenta at the bottom are essentially the same for either data choice (as is Γ).

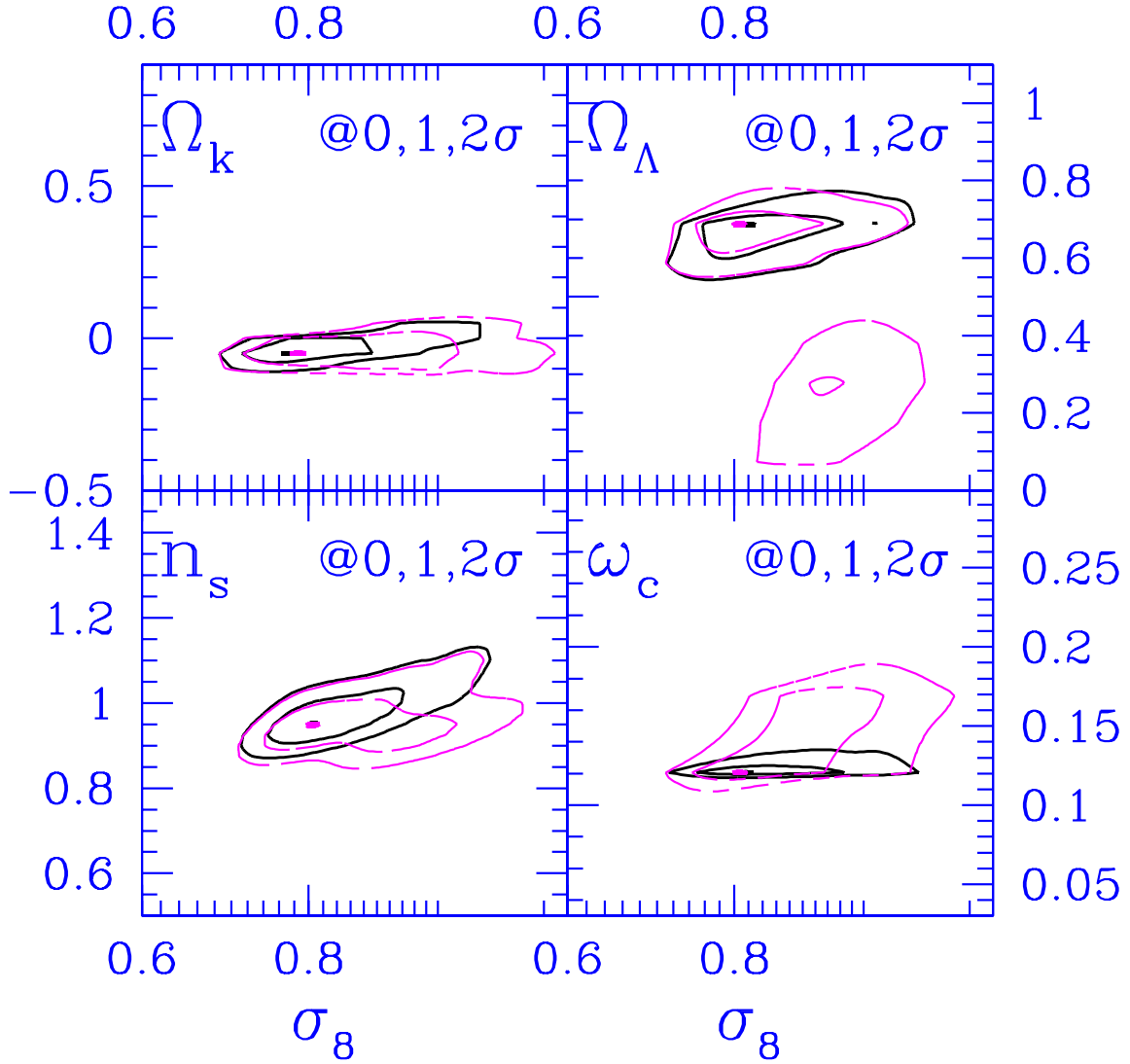


Fig. 7.— One and two sigma contours of 2D projected likelihood functions show how various cosmological parameters correlate with σ_8 . For this case, “ALL-data” was used: April 99+TOCO+B97+DASI+MAXIMA+BOOMERANG+ the CBI mosaic data for the odd $\Delta L=140$ binning. The $\Omega_k - \sigma_8$ panel shows the wk- h prior (magenta) and LSS+wk- h prior (solid/black). For the other 3 panels the flat constraint was added to these two priors as well. Note the positive correlation with n_s , but little correlation in other variables.

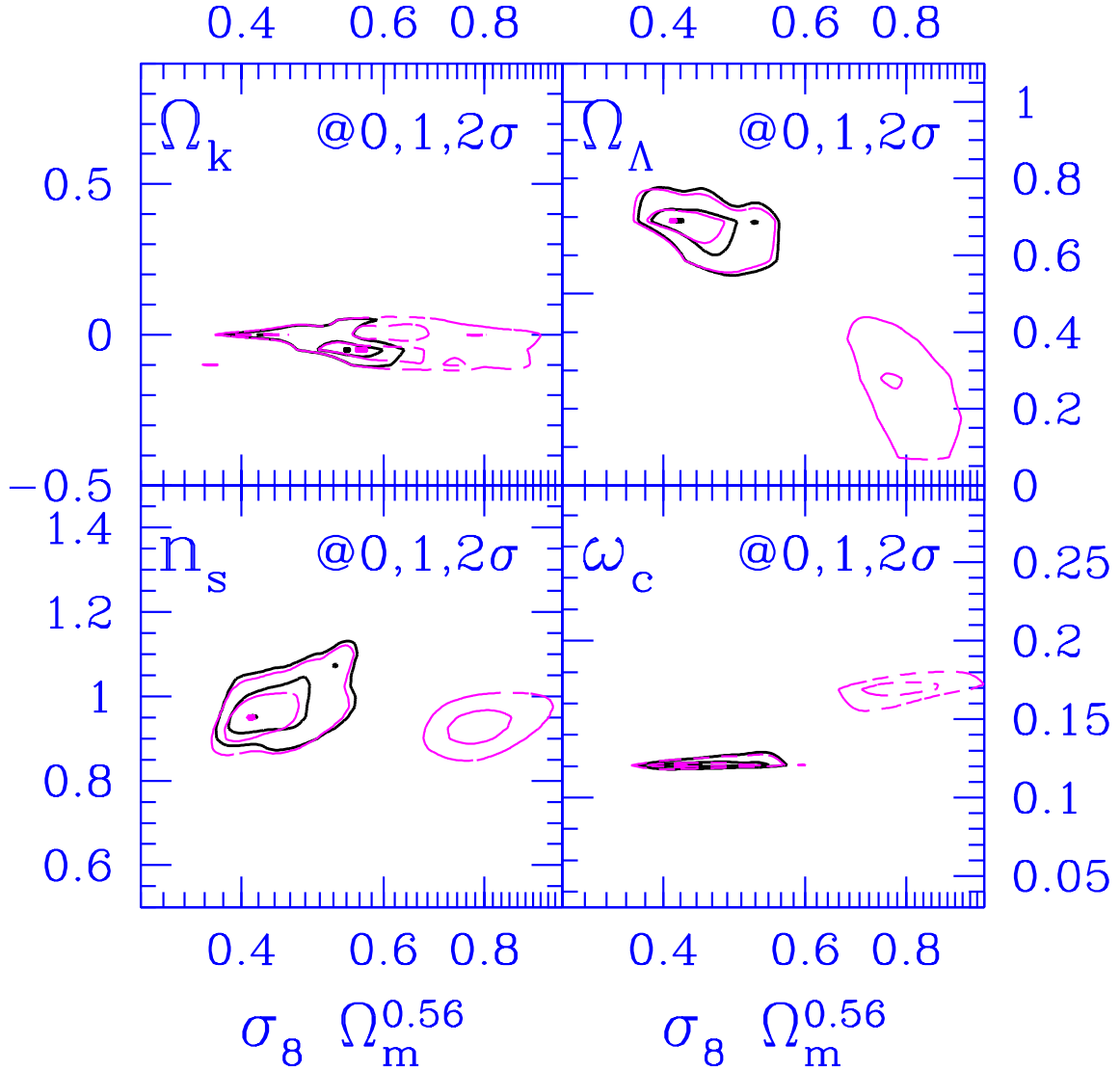


Fig. 8.— Same as Fig. 7, showing the correlations of the four cosmological parameters with $\sigma_8 \Omega_m^{0.56}$. Here the multiple solutions not evident in the σ_8 1D likelihood plots are seen. These regions are cut off by the LSS prior, by the SN prior, or by the HST- h prior.

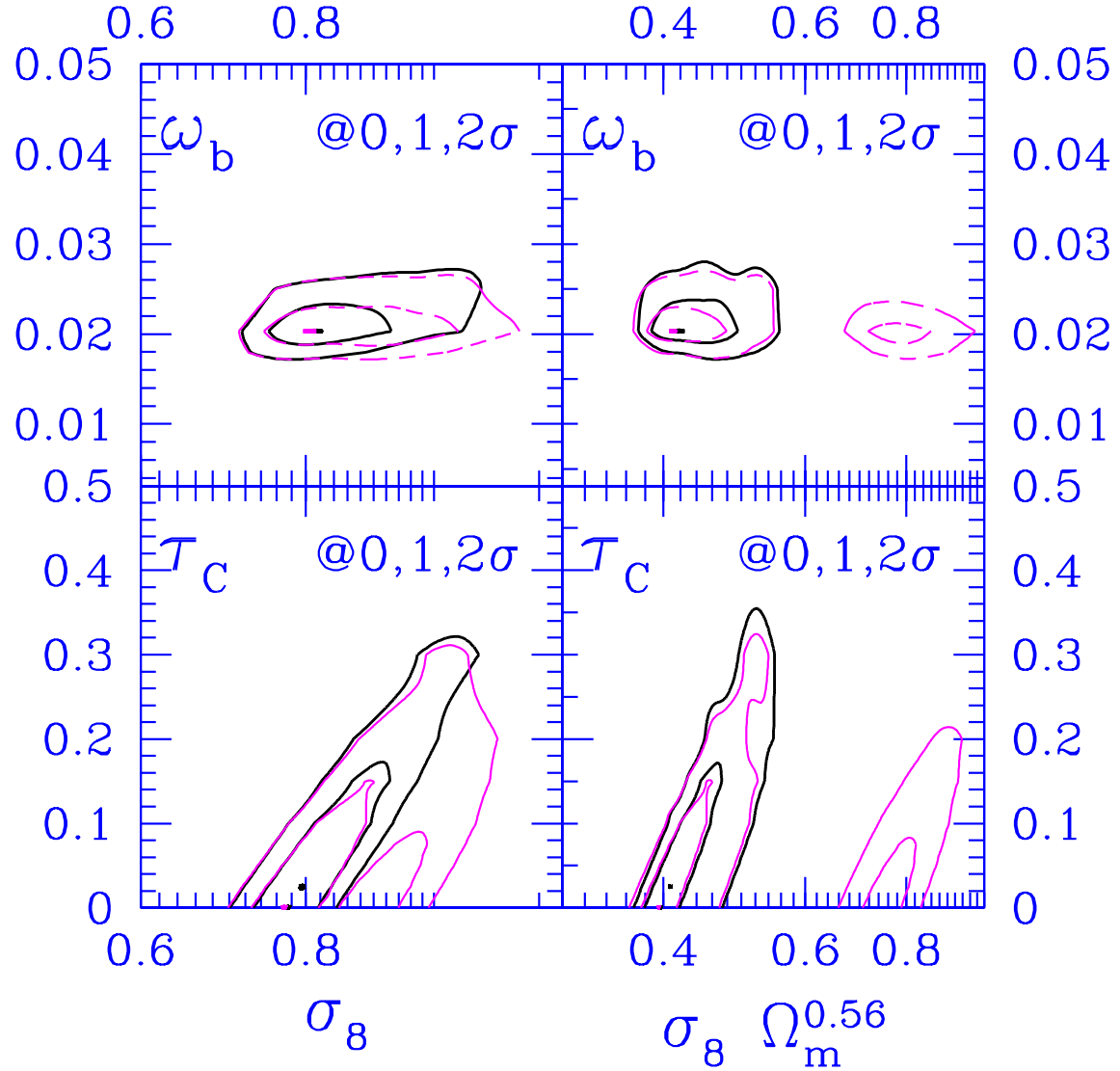


Fig. 9.— One and two sigma contours of 2D projected likelihood functions for ω_b and τ_C . The flat+wk-h prior (magenta) and flat+LSS+wk-h prior (solid/black) cases are shown. The significant σ_8 – τ_C correlation is evident, which results in a higher σ_8 for higher τ_C . One could impose a stronger prior than $\tau_C < 0.5$ (as is done here) based on astrophysical arguments. However this is fraught with uncertainty since it involves the first objects collapsing on small scales in the universe and their efficiency in generating stars that produce ionizing radiation.

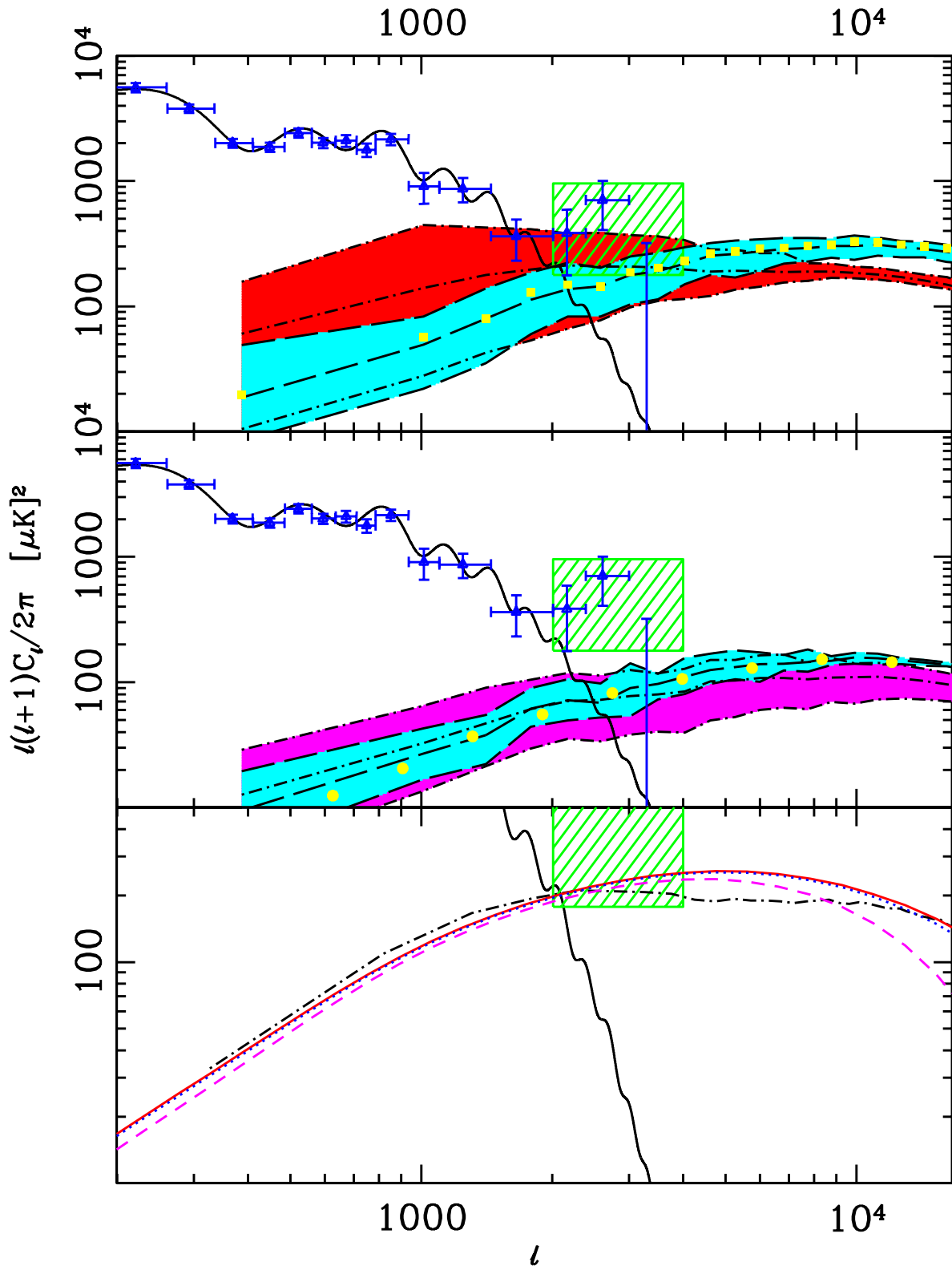


Fig. 10.— SZ power spectra for various simulations. All SZ spectra have been scaled to a common $\omega_b = 0.022$, the best-fit to the CMB data. The upper panel shows the SZ spectra for the $\sigma_8 = 1.0$ SPH 256^3 200 Mpc (cyan) and MMH 512^3 140 Mpc (red) simulations. We also plot the power spectrum from the $\sigma_8 = 0.9$ SPH 256^3 200 Mpc run (yellow points) scaled using the relation of equation 6. The target 2-sigma region suggested by the deep data is shown as a green-hatched box. An optimal power spectrum combining all CBI data with the BOOMERANG, *COBE*-DMR, DASI and MAXIMA data is shown as blue triangles. The solid black curve is a best-fit model to the data out to $\ell = 2000$. The middle panel compares the $\sigma_8 = 0.9$ 512^3 400 Mpc (cyan) and 256^3 200 Mpc (magenta) SPH simulations. The yellow points are the spectra derived from the Λ CDM simulation of Springel, White & Hernquist (2001), also scaled to $\omega_b = 0.022$. The bottom panel compares the MMH results (dot-dash) with the analytic halo model results described in § 4 for mass cuts of $0.001M_8$ (solid, red), $0.01M_8$ (dotted, blue) and $0.1M_8$ (dashed, magenta) described in the text. There is little sensitivity to a change in the lattice size over the ℓ -range shown. We note that physical effects, such as early entropy injection, may change the effective mass cut.

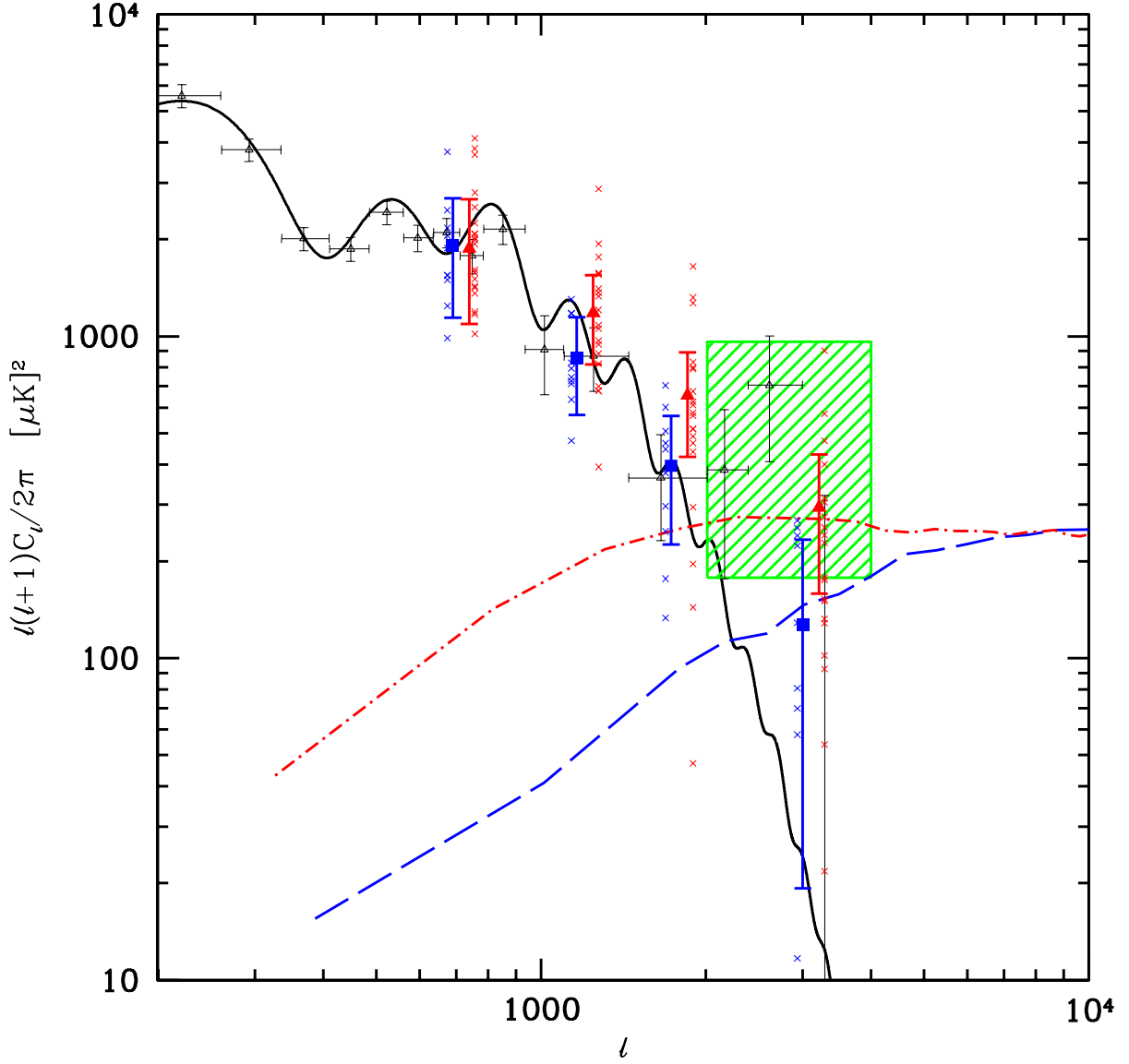


Fig. 11.— Simulated observations of CMB *plus* SZ fields. The result of band power estimation on simulated observations of the 08^h deep field containing noise, realizations of a fiducial Λ CDM model shown in black (solid line) and SZ foregrounds from the SPH and MMH $\sigma_8 = 1.0$ simulations. The blue (dashed) curve shows the average power spectrum of the input SPH maps and red (dash-dotted) is the average power spectrum of the input MMH maps. The red (triangle) points are the average band powers obtained from the analysis of 20 separate observations using the MMH maps. The blue (square) points are the average band power obtained from 10 SPH maps. The band power estimation pipeline recovers the correct power in the SZ dominated region $\ell > 2000$. The green (shaded) rectangle shows the 95% confidence region for the high- ℓ CBI deep field result. Both the MMH and SPH codes show power consistent with the confidence region.

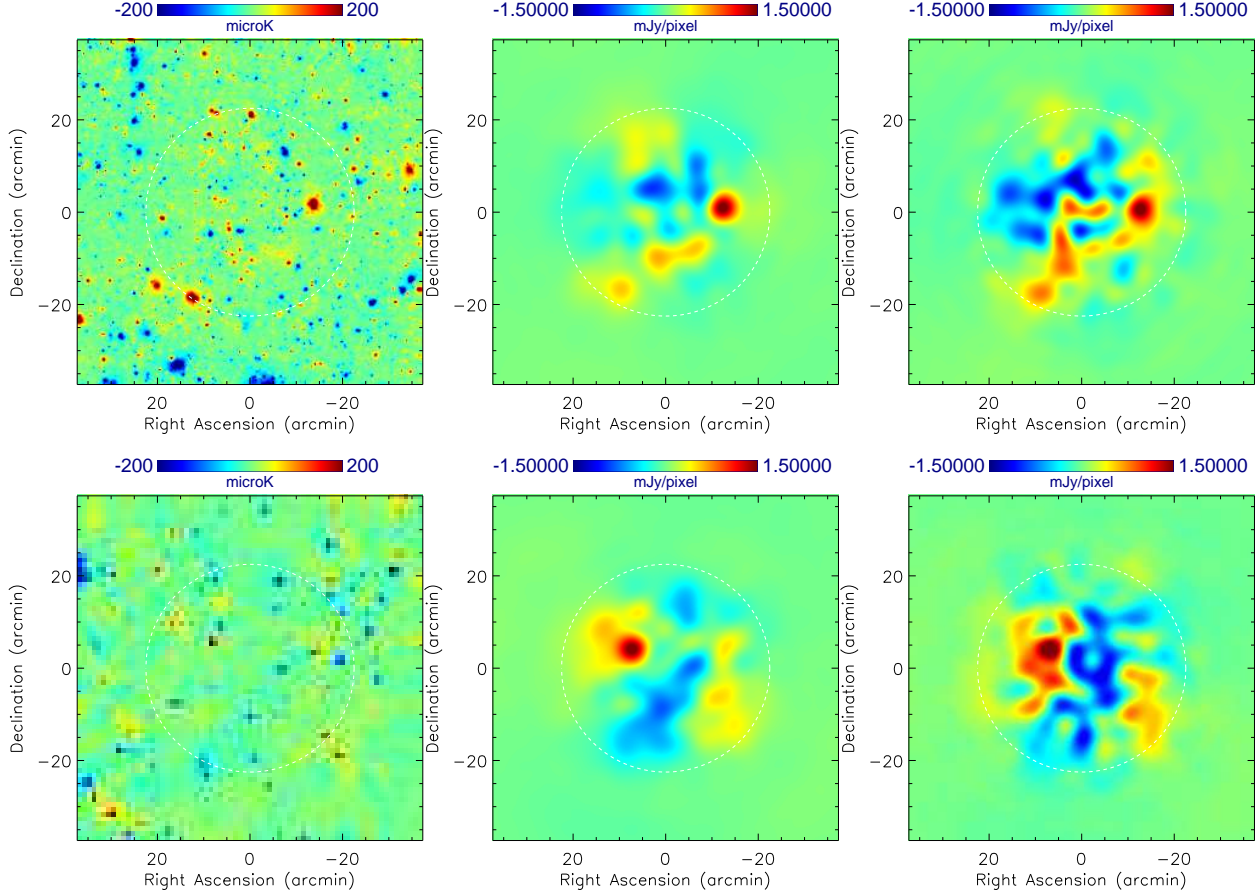


Fig. 12.— Simulated observations of SZ signals. A single SZ realization is shown for the SPH (top left) and MMH (bottom left) simulations. The area represents a (*lead-trail*) differenced field used as the signal in a simulated observation of the 08^{h} deep field. The maps are used to generate mock data sets with exact replications of the *uv*–coverage as the real data which are then filtered using the respective SZ templates. Mocks with close to negligible noise levels (top and bottom centre) show the direct representation of the CBI processed input maps. The same realization but with the same noise levels as the observed data is in the top and bottom right panels. To within the accuracy allowed by the noise, the filtered images successfully reproduce the features of the input maps within the primary beam area.

Table 1. Simulation parameters

Code	Size (Mpc)	Resolution	σ_8	$\Omega_b h^2$	Ω_Λ	Ω_m	h	n_s	Γ_{eff}
SPH	200	256^3	0.9	0.0200	0.70	0.30	0.70	1.0	0.18
SPH	200	256^3	1.0	0.0200	0.70	0.30	0.70	1.0	0.18
SPH	400	512^3	0.9	0.0220	0.70	0.30	0.70	1.0	0.18
MMH	143	512^3	1.0	0.0245	0.63	0.37	0.70	1.0	0.21

Table 2. Amplitude and Shape Parameters for LSS from the CMB: “all-data”

Priors	σ_8	$\sigma_8 \Omega_m^{0.56}$	Γ_{eq}	Γ	Γ_{eff}
wk- h	$0.92_{-0.16}^{+0.13}$	$0.65_{-0.15}^{+0.15}$	$0.28_{-0.05}^{+0.05}$	$0.20_{-0.04}^{+0.04}$	$0.21_{-0.04}^{+0.04}$
wk- h +LSS	$0.82_{-0.08}^{+0.13}$	$0.55_{-0.10}^{+0.05}$	$0.24_{-0.04}^{+0.04}$	$0.18_{-0.03}^{+0.03}$	$0.18_{-0.03}^{+0.03}$
wk- h +SN	$0.89_{-0.12}^{+0.14}$	$0.50_{-0.08}^{+0.11}$	$0.22_{-0.03}^{+0.03}$	$0.16_{-0.02}^{+0.02}$	$0.17_{-0.03}^{+0.03}$
wk- h +LSS+SN	$0.88_{-0.10}^{+0.14}$	$0.50_{-0.07}^{+0.07}$	$0.21_{-0.02}^{+0.02}$	$0.16_{-0.02}^{+0.02}$	$0.17_{-0.03}^{+0.03}$
flat+wk- h	$0.90_{-0.13}^{+0.12}$	$0.52_{-0.09}^{+0.29}$	$0.26_{-0.08}^{+0.08}$	$0.20_{-0.07}^{+0.07}$	$0.20_{-0.06}^{+0.06}$
flat+wk- h +LSS	$0.88_{-0.10}^{+0.15}$	$0.49_{-0.06}^{+0.07}$	$0.21_{-0.02}^{+0.02}$	$0.16_{-0.02}^{+0.02}$	$0.17_{-0.03}^{+0.03}$
flat+wk- h +SN	$0.87_{-0.09}^{+0.15}$	$0.48_{-0.05}^{+0.08}$	$0.21_{-0.01}^{+0.01}$	$0.15_{-0.01}^{+0.01}$	$0.17_{-0.03}^{+0.03}$
flat+wk- h +LSS+SN	$0.89_{-0.10}^{+0.14}$	$0.49_{-0.06}^{+0.07}$	$0.21_{-0.01}^{+0.01}$	$0.15_{-0.01}^{+0.01}$	$0.17_{-0.03}^{+0.03}$
flat+HST- h	$0.88_{-0.10}^{+0.15}$	$0.48_{-0.06}^{+0.09}$	$0.21_{-0.03}^{+0.03}$	$0.16_{-0.03}^{+0.03}$	$0.17_{-0.04}^{+0.04}$
flat+HST- h +LSS	$0.89_{-0.10}^{+0.14}$	$0.49_{-0.06}^{+0.07}$	$0.21_{-0.01}^{+0.01}$	$0.15_{-0.01}^{+0.01}$	$0.17_{-0.03}^{+0.03}$
flat+HST- h +SN	$0.87_{-0.09}^{+0.15}$	$0.48_{-0.05}^{+0.08}$	$0.21_{-0.01}^{+0.01}$	$0.15_{-0.01}^{+0.01}$	$0.17_{-0.03}^{+0.03}$
flat+HST- h +LSS+SN	$0.89_{-0.10}^{+0.14}$	$0.49_{-0.06}^{+0.08}$	$0.21_{-0.01}^{+0.01}$	$0.15_{-0.01}^{+0.01}$	$0.17_{-0.03}^{+0.03}$

Amplitude and shape parameter estimates from various data sets, for various prior probability choices and using all currently available CMB data: April 99+TOCO+B97+DASI+MAXIMA(3arcmin pixel results) + BOOMERANG(for the Netterfield et al. 2001 cut) and CBI mosaic data for the odd $\Delta L=140$ binning (see Paper III). In the first four rows, the weak prior in h ($0.45 < h < 0.90$) is imposed (including further weak constraints on cosmological age, $t_0 > 10$ Gyr, and matter density, $\Omega_m > 0.1$). The sequence shows what happens when LSS, SN and LSS+SN priors are imposed. While the first four rows allow Ω_{tot} to be free, the next four have Ω_{tot} pegged to unity, a number strongly suggested by the CMB data. The final 4 rows show the “strong- h ” prior, a Gaussian centered on $h = 0.71$ with dispersion ± 0.07 , obtained for the Hubble key project. The $t_0 > 10$ Gyr and $\Omega_m > 0.1$ constraints are also imposed, but they have no impact. Central values and 1σ limits for the 7 database parameters that form our fiducial minimal-inflation model set are found from the 16%, 50% and 84% integrals of the marginalized likelihood for σ_8 and $\sigma_8 \Omega_m^{0.56}$. For $\Gamma_{eq} \equiv \Omega_m h$, Γ and Γ_{eff} , the values are means and variances of the variables calculated over the full probability distribution.

Table 3. Amplitude and Shape Parameters for LSS from the CMB: CBI+DASI+BOOMERANG

Priors	σ_8	$\sigma_8 \Omega_m^{0.56}$	Γ_{eq}	Γ	Γ_{eff}
wk- h	$0.88_{-0.13}^{+0.14}$	$0.62_{-0.15}^{+0.16}$	$0.28_{-0.06}^{+0.06}$	$0.21_{-0.05}^{+0.05}$	$0.19_{-0.05}^{+0.05}$
wk- h +LSS	$0.81_{-0.07}^{+0.11}$	$0.55_{-0.10}^{+0.05}$	$0.25_{-0.04}^{+0.04}$	$0.19_{-0.03}^{+0.03}$	$0.17_{-0.03}^{+0.03}$
wk- h +SN	$0.84_{-0.08}^{+0.15}$	$0.47_{-0.06}^{+0.11}$	$0.21_{-0.03}^{+0.03}$	$0.16_{-0.03}^{+0.03}$	$0.15_{-0.04}^{+0.04}$
wk- h +LSS+SN	$0.85_{-0.08}^{+0.13}$	$0.48_{-0.06}^{+0.08}$	$0.21_{-0.03}^{+0.03}$	$0.16_{-0.03}^{+0.03}$	$0.15_{-0.03}^{+0.03}$
<hr/>					
flat+wk- h	$0.88_{-0.11}^{+0.12}$	$0.51_{-0.08}^{+0.32}$	$0.27_{-0.09}^{+0.09}$	$0.21_{-0.07}^{+0.07}$	$0.19_{-0.07}^{+0.07}$
flat+wk- h +LSS	$0.84_{-0.07}^{+0.11}$	$0.48_{-0.05}^{+0.06}$	$0.21_{-0.02}^{+0.02}$	$0.16_{-0.02}^{+0.02}$	$0.15_{-0.03}^{+0.03}$
flat+wk- h +SN	$0.83_{-0.06}^{+0.10}$	$0.46_{-0.04}^{+0.06}$	$0.21_{-0.01}^{+0.01}$	$0.16_{-0.01}^{+0.01}$	$0.14_{-0.03}^{+0.03}$
flat+wk- h +LSS+SN	$0.85_{-0.07}^{+0.11}$	$0.47_{-0.04}^{+0.06}$	$0.21_{-0.01}^{+0.01}$	$0.16_{-0.01}^{+0.01}$	$0.15_{-0.03}^{+0.03}$
<hr/>					
flat+HST- h	$0.84_{-0.07}^{+0.11}$	$0.46_{-0.04}^{+0.07}$	$0.21_{-0.03}^{+0.03}$	$0.16_{-0.03}^{+0.03}$	$0.15_{-0.04}^{+0.04}$
flat+HST- h +LSS	$0.85_{-0.07}^{+0.11}$	$0.47_{-0.04}^{+0.06}$	$0.21_{-0.01}^{+0.01}$	$0.16_{-0.01}^{+0.01}$	$0.15_{-0.03}^{+0.03}$
flat+HST- h +SN	$0.83_{-0.06}^{+0.10}$	$0.46_{-0.04}^{+0.06}$	$0.21_{-0.01}^{+0.01}$	$0.16_{-0.01}^{+0.01}$	$0.14_{-0.03}^{+0.03}$
flat+HST- h +LSS+SN	$0.85_{-0.07}^{+0.11}$	$0.47_{-0.04}^{+0.06}$	$0.21_{-0.01}^{+0.01}$	$0.16_{-0.01}^{+0.01}$	$0.15_{-0.03}^{+0.03}$

· Similar to Table. 2 but for a subset of the experimental data. We include only *COBE*–DMR, CBI, DASI and BOOMERANG data to contrast with the “all-data” compilation